



Contents lists available at ScienceDirect

Journal of Quantitative Spectroscopy & Radiative Transfer

journal homepage: www.elsevier.com/locate/jqsrt

Can multi-angular polarimetric measurements in the oxygen-A and B bands improve the retrieval of aerosol vertical distribution?



Xi Chen^a, Xiaoguang Xu^b, Jun Wang^{a,*}, David J. Diner^c

^a Department of Chemical and Biochemical Engineering, University of Iowa, Iowa City, IA 52242, USA

^b Joint Center for Earth Systems Technology, University of Maryland – Baltimore County, Baltimore, MD 21250, USA

^c Jet Propulsion Laboratory, California Institute of Technology, NASA, Pasadena, CA 91109, USA

ARTICLE INFO

Article history:

Received 21 October 2020

Revised 18 March 2021

Accepted 29 March 2021

Available online 26 April 2021

ABSTRACT

Based on the multi-angle measurements at the top of the atmosphere including radiance and polarization in O₂ A and B absorption bands simulated by forward model UNL-VRTM, the information content and posterior uncertainties about the altitude of peak aerosol extinction (H_{peak}) and half-width (w) characterizing quasi-Gaussian aerosol vertical profiles are analyzed for different observation combinations. Although the information content described as degree of freedom for signal (DFS) for H_{peak} and w increases with the number of angles, this increase reaches a limit when more than around six angles are used, regardless of surface type (ocean, vegetation or soil). Due to high surface reflectance of vegetation in O₂ A band, the DFS of H_{peak} from multi-angle measurements could be lower than 0.8, whereas the DFS > 0.9 for soil and ocean. At a single angle, polarization measurement is more sensitive to H_{peak} than radiance when H_{peak} is near the surface. Compared with single-angle radiance in O₂ A band, adding multi-angle radiances reduces retrieval uncertainty for H_{peak} by 10–20%, larger than that from only adding polarization at a single angle (< 10%), especially over vegetation. Over vegetated surface, the multi-angle radiances in O₂ A and B band have comparable information, whereas for single angle, O₂ B band has richer information than O₂ A, especially for lower H_{peak} . Multi-angle radiances and polarization in the O₂ A band as well as radiances in O₂ B band reduce the posterior uncertainty of w more than H_{peak} , especially at large AOD, while the polarized measurements in O₂ B band are more useful for H_{peak} retrieval. The most significant impact of O₂ B band radiances is to mitigate aerosol height retrieval uncertainties due to uncertainties in the surface parameters, whereas polarized measurements reduce errors from all error sources including measurements and forward model parameters.

© 2021 Elsevier Ltd. All rights reserved.

1. Introduction

Vertical distribution is an essential factor that determines how aerosols influence Earth's energy budget, the structure of atmospheric boundary layer, cloud physics, surface air quality, and atmospheric visibility. In particular, the height of aerosol layers strongly influences the magnitude and even the sign of aerosol radiative forcing in both the shortwave and longwave spectral regions [30,55]. The vertical distribution of the absorption by smoke and dust aerosols affects air temperature profiles, so that the atmospheric stability in the boundary layer and free troposphere is influenced [43]. Moreover, given increasing attention to surface particular matter (PM) pollution, aerosol height information is impor-

tant for accurately transforming columnar aerosol loading such as aerosol optical depth (AOD, commonly measured by satellite remote sensing) into surface PM_{2.5} concentrations [39]. Furthermore, plume heights are needed by chemistry transport models (CTM) to distribute the emission of smoke and dust particles in the vertical (such as in the case of simulation of smoke aerosols from fires) [5,51]. Therefore, the estimation of aerosol layer height (ALH) is of high interest and critical importance to both remote sensing and atmospheric modelling research.

Satellite remote sensing enables measurements of aerosol height information at global scale. Space-borne lidar, such as Cloud-Aerosol Lidar with Orthogonal Polarization (CALIOP) [44], measures backscattering at each vertical layer using active remote sensing, allowing detailed aerosol extinction coefficient profiles to be derived based on the backscatter ratio. However, this technique suffers from limited spatial coverage due to its narrow swath. In contrast, while not being able to provide aerosol vertical distribution information with the same level of accuracy or resolution as

* Correspondence author.

E-mail addresses: xi-chen-4@uiowa.edu (X. Chen), jun-wang-1@uiowa.edu (J. Wang).

lidar, passive remote sensing techniques utilizing observations in the ultraviolet (UV), visible/near-infrared (VNIR) and thermal infrared (TIR) bands can retrieve ALH with much more (and often nearly globally) spatial coverage and higher temporal resolution, as summarized in a review [48]. Top-of-the-atmosphere (TOA) radiance in the UV is sensitive to ALH for absorbing aerosols due to the strong and well-characterized vertical profile of Rayleigh scattering [38]. Differences in polarized scattering of light by aerosols and gas molecules provides another avenue for retrieving ALH by combining polarization in UV and near-UV blue bands [45]. Taking into account the sensitivity of polarized measurements to aerosol microphysical properties [26,47], some algorithms have been developed to retrieve ALH with particle size distribution and refractive index simultaneously [13,19,45]. Spaceborne stereo imaging, e.g., from the Multi-angle Imaging SpectroRadiometer (MISR), enables the retrieval of both heights and motion vectors of aerosols [29], but this technique is limited to distinct plumes with spatial contrasts so that parallax can be derived from pattern matching.

Satellite-based NIR measurements in oxygen (O_2) absorption bands provides another approach for passive retrieval of ALH, and is not limited to absorbing aerosols or plumes. Due to scattering of sunlight by aerosol particles, light travels through a longer atmospheric path length for lower layer of aerosols compared with higher layer, causing more absorption by O_2 molecules and resulting in less radiance exiting the TOA. Consequently, the ratio of TOA reflectance between channels inside and outside O_2 absorption band presents sensitivity to ALH. This approach has been used to retrieve ALH over dark surfaces with the Medium Resolution Imaging Spectrometer (MERIS), Polarization and Directionality of the Earth's Reflectances (POLDER) and Earth Polychromatic Imaging Camera (EPIC) [14,49]. The ALH sensitive O_2 A band is also involved in the carbon dioxide monitoring from space to correct the interference from aerosol scattering simultaneously, such as for OCO-2, GOSAT and TanSat [36,54,2]. Besides the commonly-used O_2 A band at 755–775 nm, observations in the O_2 B band (685–695 nm) offer the advantage in ALH retrieval over land due to much lower surface reflectance compared to the O_2 A band, particularly over vegetation [10,50]. Hyperspectral observations in O_2 absorption bands, e.g., from SCanning Imaging Absorption SpectroMeter for Atmospheric CHartography (SCIAMACHY), Global Ozone Monitoring Experiment-2 (GOME-2), and TROPOspheric Monitoring Instrument (TROPOMI) potentially provide additional details about aerosol height [17,22,28,34].

The aim of this study is to analyze the information content about ALH in the multi-angle measurements of backscattered polarization and radiance at the TOA, especially in the O_2 A and B absorption bands. Even though there has been instrument detecting polarization in O_2 A band, such as the Thermal and Near-infrared Sensor for Carbon Observation-Fourier Transform Spectrometer (TANSO-FTS) onboard the Greenhouse Gases Observing Satellite (GOSAT), these measurements are only from single angle and their potential usage in ALH study was not fully explored [52]. Our research is motivated by the lack of measurements in O_2 bands from multiple angles, considering more information characterizing aerosol properties can be provided by multi-angle measurements. For example, the measurements in four visible and near-infrared bands at nine discrete viewing geometries of MISR are used to retrieve both AOD and aerosol types due to the sensitivity of multi-angle radiance observations to the aerosol scattering phase functions, which are governed by particle size, shape and composition [7,21]. Besides radiance, multi-angle polarization observations, such as from POLDER, also enhance the capability to distinguish aerosol components [13,18,46]. Therefore, focusing on ALH retrieval, the question arises: how might the combination of radiance and polarization measurements in O_2 bands from multi-

ple angles improve the ALH information? Specifically, several questions are posed in this paper:

- Compared with the single-angle measurement like from EPIC and TROPOMI, to what degree is information content about ALH improved by the multi-angle radiances in O_2 A band, such as those to be observed by the future Multi-Angle Imager for Aerosols (MAIA) instrument [6,7]?
- Since adding polarization measurements in O_2 absorption band from single view angle has been proved to benefit ALH retrieval over bright surfaces [1,10,40], how much would adding multi-angle polarization measurements in the O_2 A band improve the information content of ALH?
- Considering the advantages of lower surface reflectance in O_2 B band, how will the ALH information content change when combining multi-angle radiance and polarization observations in the O_2 B band with the A band? This question is relevant to whether a similar multi-angle polarimeter like SPEXone, part of the Plankton, Aerosol, Cloud, ocean Ecosystem (PACE) mission scheduled to launch in the 2022–2023 timeframe, but with higher spectral resolution of polarization observation to resolve O_2 absorption is necessary to retrieve ALH.
- How do the results for (a)–(c) depend on the number of view angles?

To address these questions, we conducted a comprehensive theoretical analysis to quantify the ALH information provided by multi-angle and polarimetric measurements in the O_2 A and B bands. Such analysis is based on MAIA synthetic data simulated by the Unified Linearized Vector Radiative Transfer model (UNL-VRTM, [40,50]) for various aerosol types and observation scenarios. Details about the theoretical basis and simulation assumptions are stated in Sections 2 and 3, respectively. Section 4 compares the quantitative information content of ALH parameters provided by multi-angle polarimetric observations with different number of viewing geometries and different surface and aerosol types. Each role of multi-angle, polarized and O_2 B band measurements in ALH retrieval is quantified in Section 5, along with the impact of model parameter uncertainties. Section 6 summarizes the conclusions and suggests some useful sensor design considerations aimed at improving aerosol height remote sensing.

2. Methodology

Information content analysis is an effective method to provide first-order analysis of the capability of satellite or ground-based measurements to retrieve the atmospheric variables of interest. It has been demonstrated to be valuable for satellite sensor design and retrieval algorithm development [3,10,15,16,47,20]. The advantage of this method is that the retrieval capability can be quantified without invoking the development of real retrieval algorithm; rather, it provides a top-level physics-based guidance on algorithm design. This approach is based on the optimal estimation theory proposed by Rodgers [32], which is briefly reviewed in Section 2.1, while implementation of this approach in this study is introduced in Section 2.2.

2.1. Optimal estimation theory

In optimal estimation theory, the relationship of the state vector \mathbf{x} consisting of n parameters to be retrieved and an observation vector \mathbf{y} containing m measurements is as follows:

$$\mathbf{y} = \mathbf{F}(\mathbf{x}) + \boldsymbol{\epsilon}. \quad (1)$$

In this equation, \mathbf{F} is a forward model (in this case, the UNL-VRTM) describing the physical process relating the satellite observations and the atmospheric parameters (such as aerosol optical

depth). ϵ represents the errors from the simulation of forward model and satellite measurements. The sensitivity of the forward model with respect to \mathbf{x} is captured by the weighting functions (Jacobians matrix), which can be expressed as: $\mathbf{K} = \frac{\partial \mathbf{F}}{\partial \mathbf{x}}$. The prior uncertainty of the state vector can be described by the prior error covariance matrix \mathbf{S}_a . Assuming the probability density function (pdf) of the errors (ϵ) to follow Gaussian distributions, based on Bayes' theorem the posterior pdf can be derived by updating the prior pdf with a measurement pdf. Therefore, utilizing the observation error covariance matrix \mathbf{S}_ϵ , the retrieval error covariance matrix can be derived as:

$$\hat{\mathbf{S}}^{-1} = \mathbf{K}^T \mathbf{S}_\epsilon^{-1} \mathbf{K} + \mathbf{S}_a^{-1}. \quad (2)$$

The observation error covariance matrix is defined as a sum of two parts:

$$\mathbf{S}_\epsilon = \mathbf{S}_m + \mathbf{S}_y, \quad (3)$$

one of which is the error covariance matrix describing the uncertainties of satellite measurements (\mathbf{S}_y), such as the radiometric calibration error. \mathbf{S}_m represents the forward model errors resulting from model parameters (\mathbf{b}) that are not retrieved but significantly affect the forward model simulation. \mathbf{S}_m can be calculated by using the error covariance matrix and Jacobian matrix for parameters in \mathbf{b} , denoted respectively as \mathbf{S}_b and \mathbf{K}_b in below:

$$\mathbf{S}_m = \mathbf{K}_b^T \mathbf{S}_b \mathbf{K}_b. \quad (4)$$

In addition to the posterior error covariance matrix, the averaging kernel matrix \mathbf{A} is another variable to quantify the information about retrieved parameters from observations, and is defined as the derivative of the retrieved state with respect to the true state in Eq. (5):

$$\mathbf{A} = \frac{\partial \hat{\mathbf{x}}}{\partial \mathbf{x}} = (\mathbf{K}^T \mathbf{S}_\epsilon^{-1} \mathbf{K} + \mathbf{S}_a^{-1})^{-1} \mathbf{K}^T \mathbf{S}_\epsilon^{-1} \mathbf{K}. \quad (5)$$

The closer each diagonal element in matrix \mathbf{A} (i.e., $\frac{\partial \hat{x}_i}{\partial x_i}$) is to 1.0, the more the retrieved state is determined by the measurements instead of the a prior. Ideally, if the forward model fully describes the physics of the real atmosphere without any approximation and retrieval is achieved after its convergence to the global minimum of cost function, averaging kernel value of 1.0 suggests the retrieved state fully reflect the true state. While in reality this is never true, larger averaging kernel still indicates more information content from satellite measurements. Therefore, the trace (sum of all diagonal elements) of averaging kernel matrix \mathbf{A} is called the degree of freedom for signal (DFS) and represents how much information about the retrieved parameters we can obtain from the satellite measurements. Correspondingly, each diagonal element describes the information for each retrieved parameter. Considering the averaging kernel describes the relative weight of the information about the state vector from the satellite measurements compared to that from the a prior, the DFS value depends on the a prior uncertainty assumption. In other words, if we define a large prior uncertainty, DFS from the same satellite observations will increase compared to small prior uncertainty, whereas this does not mean the retrieval becomes more capable. Therefore, in this study, we also investigate the posterior uncertainty compared to the prior uncertainty to quantify the ALH information provided by O_2 band satellite measurements. The Jacobians of both retrieved and ancillary parameters (\mathbf{K} and \mathbf{K}_b) are simulated by the model, while the error covariance matrices are defined empirically (Section 3.2.2).

2.2. Radiative transfer simulation

Satellite observations and corresponding weighting functions with respect to retrieved parameters are simulated by UNL-VRM

at multiple viewing geometries. UNL-VRM is based on the VLI-DORT model for calculating the Stokes vector $[I, Q, U, V]^T$, where I represents radiance, Q and U describe the linear polarization components, and V describes the circular polarization. We consider an observation vector comprising I and the degree of linear polarization (DOLP), where DOLP is defined by:

$$\text{DOLP} = \frac{\sqrt{Q^2 + U^2}}{I}. \quad (6)$$

The physics describing the impact of aerosol vertical distribution on the TOA radiance at the wavelength where oxygen (O_2) has absorption has become the subject of many studies; fewer papers, such as [10,40,53], have explored the relationship between polarization in O_2 absorption bands and aerosol height. Since Rayleigh scattering often induces positive and strong DOLP while spherical aerosols may generate less positive or negative DOLP at different scattering angles. However, in the O_2 absorption band aerosol scattering at lower atmosphere can be suppressed by O_2 absorption, the resulting DOLP at TOA is dominant by Rayleigh scattering. In other words, the light scattered by a lower aerosol layer goes through more O_2 absorption, so that Rayleigh scattering has greater contribution on TOA DOLP. Therefore, DOLP in O_2 absorption bands is also sensitive to ALH. Using subscript a to represent value in an O_2 absorption band, with superscript A or B representing the specific band, the measurement vector \mathbf{y} at single viewing angle is defined as:

$$\mathbf{y} = [I_a^A, I_a^B, \text{DOLP}_a^A, \text{DOLP}_a^B]^T. \quad (7)$$

For retrievals using only radiance in the O_2 A band, \mathbf{y} consists of one element (I_a^A). If polarization in O_2 A band is added into the measurement vector, \mathbf{y} has two elements, and so on. Given N multi-angle measurements, the total number of observations is multiplied by the number of view angles:

$$\mathbf{y}_m = [y_1^T, y_2^T, y_3^T, \dots, y_N^T]^T. \quad (8)$$

In the information content analysis, no real retrieval process needs to be conducted and radiative transfer simulations are used as the measurement vector instead. In other words, the true state for the measurement vector is already known and the Jacobians (\mathbf{K} and \mathbf{K}_b) are simulated on the true state. Thus, the a prior of the state vector is not necessary in this analysis and the DFS and retrieval uncertainty only depend on the prior uncertainty as shown in Eq. (2)-(5).

3. Instrument and simulation assumptions

The instrument to be studied is a hypothetical successor to MAIA with additional multiple-angle capability to measure polarization in O_2 A and B bands; here we refer this instrument as Multi-Angle Polarization Measurements with Oxygen band (MAPMO). The characteristics of MAPMO and underlying assumptions of our simulations including aerosol properties, surface reflectance, and prior and observation error covariance matrices are described in this section. Furthermore, to analyse the roles of multi-angle and polarized measurements in ALH retrieval, the different scenarios combining different measurements are defined as well.

3.1. Instrument characteristics of MAIA and MAPMO

The MAIA instrument was selected by the NASA Earth Venture Instrument program in early 2016 to study the adverse health effects of airborne PM [7]. To improve the capability of MISR for monitoring aerosol particle properties, MAIA's design incorporates polarimetry in three of its 14 spectral bands, which extend from

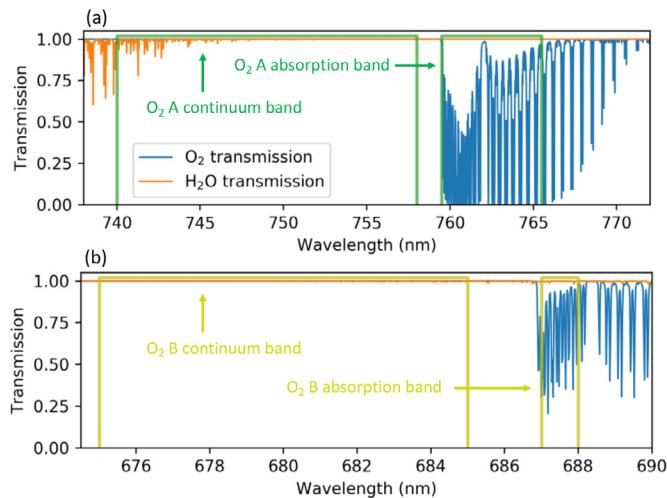


Fig. 1. Assumed square-shaped spectral filter functions for a) MAIA O₂ A and b) MAPMO O₂ B absorption band. The O₂ and H₂O transmission lines are shown in both a) and b). The left square bandpass in each panel shows the assumed spectral filter for the O₂ continuum band and the right one is for the O₂ absorption band.

the UV (365 nm) to the shortwave infrared (2125 nm) bands. The nadir footprint is approximately 200 m. MAIA's 14 bands include radiance measurements in and out of the O₂ A band (Fig. 1a), centered at 762.5 nm and 749 nm, with full-width at half-maximum (FWHM) of 6 and 18 nm, respectively. In this study, we approximate the spectral filter function for these bands with a square-box shape. Even though the square shape assumption is simple and not realistic, we found that assuming a Gaussian shape response function (closer to real instrument) results in close convolved TOA observation and Jacobians with negligible difference (see Appendix). Thus, square spectral response function assumption will not affect our information content estimation. MAIA will also make highly accurate polarimetric measurements with ± 0.005 DOLP uncertainty at 442, 645, and 1040 nm. The MAPMO concept adds polarimetric observations in O₂ A band, with similar DOLP accuracy as in the MAIA polarimetric bands. Moreover, for MAPMO, the radiance and polarized measurements centered at 680 nm and 688 nm (O₂ B) with FWHM of 10 and 1 nm (Fig. 1b) are observed as well. We simulate the TOA spectrum with high spectral resolution, 0.02 nm in O₂ absorption band and 1.0 nm in the wing band, and then convolve them using the assumed MAIA and MAPMO square-box spectral response functions.

Instead of containing multiple cameras that point at discrete along-track viewing angles (as in MISR), MAIA uses "step-and-stare" mode to view targets from different geometries by pointing its single camera to any along-track and cross-track position within a bidirectional field of regard [7]. For this study, we assume total nine angles following typical MISR viewing geometries in the simulations, although MAIA is planned to observe 5 angles which varies with different scenes. As illustrated in Fig. 2a, the nine viewing zenith angles of 0° , $\pm 26.1^\circ$, $\pm 45.6^\circ$, $\pm 60.0^\circ$, and $\pm 70.3^\circ$ are simulated, four of which point to the forward direction (entitled Af, Bf, Cf, and Df and denoted with positive sign of zenith angle), one points towards the nadir (An), and four point to the afterward direction (Aa, Ba, Ca, and Da). The corresponding viewing azimuth angles of forward and afterward angles are assumed to keep multiple angles along the satellite track. The three solar geometries with different solar zenith angles (SZA) and azimuth angles (SAZ) (25° SZA and 123.2° SAZ, 40° SZA and 146.6° SAZ, 60.7° SZA and 163.8° SAZ) are also presented in Fig. 2a and the impact of solar geometry on ALH information will be analysed in Fig. 5. Thereafter, the

analysis and figures are only for one fixed solar geometry (40° SZA and 146.6° SAZ).

3.2. Simulation assumptions

In addition to the sensor configuration, the atmospheric profile, aerosol properties and surface reflectance are also needed as input to UNL-VRM to simulate TOA reflectance and polarization. The atmospheric temperature, pressure and trace gas vertical profiles are assumed to follow the mid-latitude summer atmospheric profiles from Optical Properties of the Atmosphere, Third Edition, AFCRL-72-0497. To increase vertical resolution, the 49-layer standard atmospheric profile is mapped to the GEOS-5 vertical grids with 47 hybrid pressure-sigma layers [56]. Given this study focusing on the simulation in O₂ absorption bands, UNL-VRM implements the cross section and spectroscopic line parameters of absorbing gases including H₂O, O₃ and O₂ from the high-resolution transmission molecular absorption database (HITRAN) [33]. Meanwhile, the continuum absorption for water vapor are calculated using the MT_CKD model developed by Mlawer, D.C. Tobin and S.A. Clough [27]. The details about each module in UNL-VRM can be found in [40,50]. Two types of aerosol model and surface model are described in Section 3.2.1. Furthermore, when applying the simulations into the ALH information content analysis, the prior error and observation error covariance matrices are assumed as described in Section 3.2.2.

3.2.1. Aerosol and surface model

Similar to [38], two typical aerosol models representing biomass burning (BB) and urban-industrial (UI) are used in our simulations to test the impact of different single-scattering properties of aerosol particles on ALH information. The microphysical parameters including effective radius (r_{eff}) and variance (v_{eff}) for a lognormal particle size distribution, as well as the refractive index for BB and UI aerosols are summarized in Table 1. Here, we assume the refractive index for each aerosol type keeps constant from O₂ B to A band. These parameters follow previous studies about climatology of AERONET inversion products during multiple years for typical aerosol types at selected sites [12]. After inputting these microphysical properties, a linearized Mie code is used to simulate the single-scattering properties of aerosols containing extinction coefficient, single scattering albedo (SSA) and 4×4 scattering phase matrix \mathbf{P} :

$$\mathbf{P} = \begin{bmatrix} P_{11} & P_{12} & 0 & 0 \\ P_{21} & P_{22} & 0 & 0 \\ 0 & 0 & P_{33} & P_{34} \\ 0 & 0 & P_{43} & P_{44} \end{bmatrix}, \quad (9)$$

where $P_{12} = P_{21}$, $P_{34} = -P_{43}$. Here, P_{11} represents the normalized phase function describing the scalar component of particle scattering, while $-P_{12}/P_{11}$ is the polarized scattering corresponding to DOLP. The SSA for these two aerosol types are also shown in Table 1, indicating the stronger absorption BB compared to UI. As shown in Figs. 2b and 2c, the wavelength dependent P_{11} and $-P_{12}/P_{11}$ of different aerosol types have different variation with scattering angle, resulting in distinct scattering characteristics influencing TOA observations by satellites. The assumed multiple viewing geometries are also highlighted in Fig. 2b and 2c, indicating different sensitivities of TOA radiance and DOLP with respect to ALH. For example, following the physical principle we mentioned in Section 2.2, for scattering angles close to 180° , such as viewing geometry Aa and Ba, the aerosol DOLP ($-P_{12}/P_{11}$) is negative for UI but positive for BB at 688 nm (Fig. 2c), which will lead to lower (higher) DOLP for stronger UI (BB) scattering when the O₂ absorption is less due to higher aerosol layer. Therefore, combining

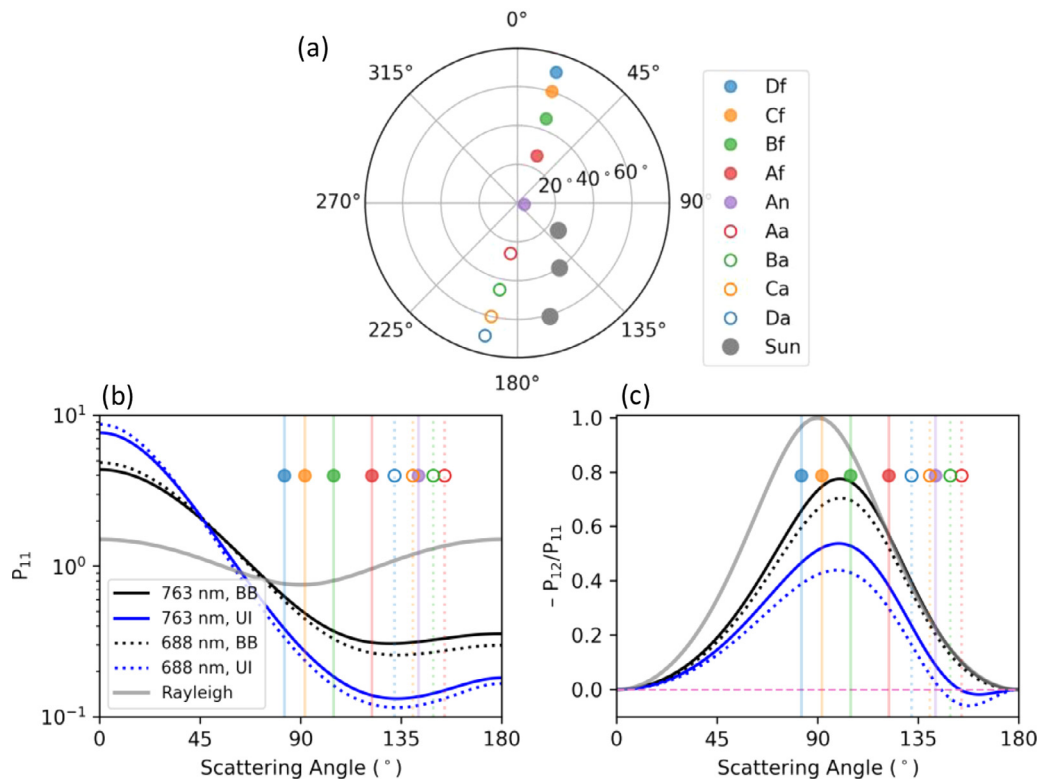


Fig. 2. a) Angular sampling assuming MISR viewing geometries in polar coordinates. The radius and polar angle represent viewing zenith angle from 0° to 80° and viewing azimuth angle from 0° to 360°, respectively. Here, 0° viewing azimuth angle is defined as the north direction. The same color dots indicate identical viewing zenith angle but the solid dots are for forward angles relative to the nadir direction (shown as An) while circles represent aftward directions. The viewing zenith angle increases from Af (or Aa) to Df (or Da). The grey dots represent three solar geometries as described in the main text. The scattering angles in panel (b) and (c) corresponding to sampled nine viewing angles are calculated from a fixed solar geometry with 40° SZA and 146.6° SAZ. b) The phase function (P_{11}) and c) DOLP of phase matrix ($-P_{12}/P_{11}$) vary with scattering angle at O₂ A (solid lines) and B bands (dotted lines) for two aerosol types BB (blue lines) and UI (black lines). The modeled aerosol microphysical parameters are shown in Table 1. The scattering angles of sampled multiple viewing geometries in b) and c) are highlighted by the same symbols as in a). The thin pink dash line in c) indicates zero DOLP.

Table 1
Microphysical and optical properties of aerosols adopted in the simulations.

Type	r_{eff} (μm)	v_{eff}	Refractive index	SSA*	Reference
Biomass burning	0.13	0.17	1.52–0.021i	0.87/0.85	[12,31]
Urban industrial	0.21	0.16	1.41–0.003i	0.98/0.98	[12]

*: The left values to the symbol “/” are for 680 nm and the right are for 749 nm, corresponding to O₂ B and A band, respectively. The UI SSA has little distinction between O₂ B and A band.

satellite measurements at various viewing geometries could provide more information about ALH due to their different sensitivities to ALH.

In the simulation, we assume the aerosol extinction vertical profile to follow quasi-Gaussian function given by two parameters:

$$\tau(z) = c \frac{\exp(-\sigma|z - H_{peak}|)}{[1 + \exp(-\sigma|z - H_{peak}|)]^2}, \quad (10)$$

one of which is the peak height (H_{peak}) where the aerosol extinction is the largest and the other σ is related to the width (w) at the half maximum of aerosol extinction. σ and w are easily transformed to each other:

$$\sigma = \frac{\ln(3 + \sqrt{8})}{w}. \quad (11)$$

To simplify, in the analysis of this paper, we use w instead of σ as the retrieved parameters together with H_{peak} . As in the EPIC ALH retrieval algorithm [50], the AOD is first fitted from measurements in atmospheric window channels and then applied in spectral fitting of O₂ absorption band observation to retrieve ALH. Therefore,

rather than retrieving aerosol concentration and absorption at each level, we only include H_{peak} and w in the state vector of our retrieval, and other aerosol related parameters (AOD and SSA) are prescribed as model parameters. As a consequence, our state vector only consists of H_{peak} and w .

ALH information in the O₂ absorption bands are critically affected by the reflectance of underlying surface [50]. It is thus important to consider a realistic representation for surface reflectance and polarization. Many studies (e.g., [24,25,57,58,59]) suggested that the polarized component of surface reflectance is quantitatively small but rather import. In this study, we use the bidirectional polarization distribution function (BPDF) together with a bidirectional reflectance distribution function (BRDF) model. Following [31], the 4 × 4 surface reflectance matrix $\mathbf{R}(\lambda, \vartheta_v, \vartheta_0, \phi)$ at wavelength λ , solar zenith angle ϑ_0 , viewing zenith angle ϑ_v and relative azimuth angle ϕ is expressed as:

$$\mathbf{R}(\lambda, \vartheta_v, \vartheta_0, \phi) = \mathbf{R}_{diff} + \mathbf{R}_{spec}, \quad (12)$$

where the matrix for diffuse unpolarized reflectance \mathbf{R}_{diff} is related to three-kernel Ross-Li BRDF model ($R_l(\lambda, \vartheta_v, \vartheta_0, \phi)$) used by MODIS

Table 2The parameters of three-kernel BRDF model and BPDF model for vegetation and soil surface at O₂ A and B bands.

Surface type	k_1^a	k_2^a	k_3^a	α^a	ν^a
vegetation	0.6637/0.0749 ^b	0.4566/0.0515	0.0577/0.0065	6.57	0.62
soil	0.1665/0.1451	0.0911/0.0794	0.0263/0.0229	6.9	0.03

^a Here k_1 , k_2 and k_3 correspond to the amplitude factors as expressed in Eq. (13) in the main text, while α represents the factor for BPDF kernel and ν is the NDVI parameter in Eq.(14).

^b The left values separated by symbol “/” are for 763 band and the right values are for 688 band.

Table 3

Simulated measurements applied in each scenario. Here, all scenarios include multi-angle measurements.

Scenarios	O ₂ A Radiance	O ₂ A Polarization	O ₂ B Radiance	O ₂ B Polarization
A-1 (MAIA)	✓	×	×	×
A-IP	✓	✓	×	×
B-1	×	×	✓	×
B-IP	×	×	✓	✓
AB-1	✓	×	✓	×
AB-IP (MAPMO)	✓	✓	✓	✓

[37,42]:

$$R_{diff} = R_I(\lambda, \vartheta_v, \vartheta_0, \phi) \begin{pmatrix} 1 & 0 & 0 & 0 \\ 0 & 0 & 0 & 0 \\ 0 & 0 & 0 & 0 \\ 0 & 0 & 0 & 0 \end{pmatrix}$$

$$= [k_1(\lambda) + k_2(\lambda)f_{geom}(\vartheta_v, \vartheta_0, \phi) + k_3(\lambda)f_{vol}(\vartheta_v, \vartheta_0, \phi)]$$

$$\times \begin{pmatrix} 1 & 0 & 0 & 0 \\ 0 & 0 & 0 & 0 \\ 0 & 0 & 0 & 0 \\ 0 & 0 & 0 & 0 \end{pmatrix}. \quad (13)$$

Here, $f_{geom}(\vartheta_v, \vartheta_0, \phi)$ and $f_{vol}(\vartheta_v, \vartheta_0, \phi)$ are two semi-empirical kernels representing volumetric and geometric-optical surface scattering of Ross-Li three-kernel model, respectively, which only depend on geometries rather than wavelength [41], while the first term represents isotropic surface reflection. Correspondingly, $k_1(\lambda)$, $k_2(\lambda)$ and $k_3(\lambda)$ are the linear combination coefficients for these kernels and depend on wavelength. The specular reflectance matrix (\mathbf{R}_{spec}) in Eq.(12) consists of empirical BPDF coefficient $R_p(\vartheta_v, \vartheta_0, \phi)$ and 4×4 Fresnel matrix $\mathbf{F}(m, \theta_r)$:

$$R_{spec} = R_p(\vartheta_v, \vartheta_0, \phi) \mathbf{F}(m, \theta_r)$$

$$= \frac{\alpha \exp(-\tan(\theta_r)) \exp(-\nu)}{4(\cos(\vartheta_v) + \cos(\vartheta_0))} \mathbf{F}(m, \theta_r). \quad (14)$$

As shown in [24], θ_r is the angle of the specular reflection related to viewing geometry, ν is the Normalized Difference Vegetation Index (NDVI) related parameter and α is free parameter. The fixed refractive index m is equal to 1.5 for the land surface. By using both radiance and polarization data from the airborne Research Scanning Polarimeter (RSP) during the Aerosol Lidar Validation Experiment (ALIVE) measurement campaign performed in Oklahoma (USA, Southern Great Plains) in September of 2005 [25], the parameters $k_1(\lambda)$, $k_2(\lambda)$ and $k_3(\lambda)$ in the BRDF model are fitted at three observed channels for both soil and vegetation surface, as in Table 2 of [24]. To apply the parameters to the O₂ absorption band, we interpolated them into O₂ A and B bands based on the spectral Lambertian albedo from the Advanced Spaceborne Thermal Emission Reflection Radiometer (ASTER) surface library. On the contrary, the BPDF model is wavelength independent, and α was only fitted for different NDVI parameters of soil and vegetation land from RSP data (Table 3 in [24]). Table 2 presents all the land surface BRDF and BPDF parameters used in our simulation.

Furthermore, to simulate the polarization of the ocean surface, a vector kernel GISS-CoxMunk based on the description in [26] is used, with two parameters related to wind speed and water refrac-

tive index. In our simulation, the wind speed is assumed to be 5 m/s and the refractive index is 1.334.

Based on the models described above, the R_{11} and R_{21} in surface reflectance matrix \mathbf{R} representing the total reflectance and polarized reflectance, respectively, are simulated and shown in Fig. 3 for two land surfaces and ocean. It is clear that for the vegetated surface, the difference of surface reflectance at different viewing geometries could reach 0.2 to 0.3 in the O₂ A band but only 0.03 to 0.04 in O₂ B band due to its intrinsically lower reflectance (Fig. 3a and 3b), resulting in less influence of surface reflectance on the sensitivity to ALH at different angles. However, for the soil surface, there is little difference between the impact on ALH sensitivity in the two bands due to their similar surface reflectance (Fig. 3d and 3e). The soil has stronger negative or positive surface polarization than vegetation, which results in a greater contribution to the TOA DOLP. The ocean surface only shows strong total and polarized surface reflectance at small sunglint angles, while at other angles they are small and change little (Fig. 3g-3i). Generally, to compare the impact of different surface types on the measurement sensitivity to ALH, we perform the simulation over three surface types: ocean, soil and vegetation, with the surface polarization taken into consideration.

3.2.2. Error covariance matrix

In addition to the calculation of analytical weighting functions of aerosol parameters from our linearized UNL-VRTM model, the assumptions about the prior error covariance matrix and the observation error covariance matrix (\mathbf{S}_a and \mathbf{S}_ϵ) are also necessary to analyze the averaging kernel matrix and posterior uncertainty of ALH, as described in Section 2.1. In the retrieval, the two parameters of ALH in the state vector are treated as independent, thus the prior error covariance matrix is defined as a 2×2 diagonal matrix, whose diagonal elements are the square of the uncertainty (σ^2) of corresponding retrieved parameters. In our analysis, both the prior uncertainties of H_{peak} and w are assumed to be 100%, which means the prior error covariance matrix is an identity matrix.

As one part of the observation uncertainty, the uncertainties of satellite measurements (S_y) involve the systematic error and random error during the instrument observation process. After on-board and vicarious calibration, the uncertainties of radiance and polarized measurements are assumed to 5% and 0.005, respectively [11]. If we ignore the correlation between different channels (O₂ A and B band) and between radiance and polarized measurements, the S_y of single-angle viewing is also defined as a diagonal matrix. However, for retrieval from multi-angle measurements, the correlation between measurement uncertainties of different viewing ge-

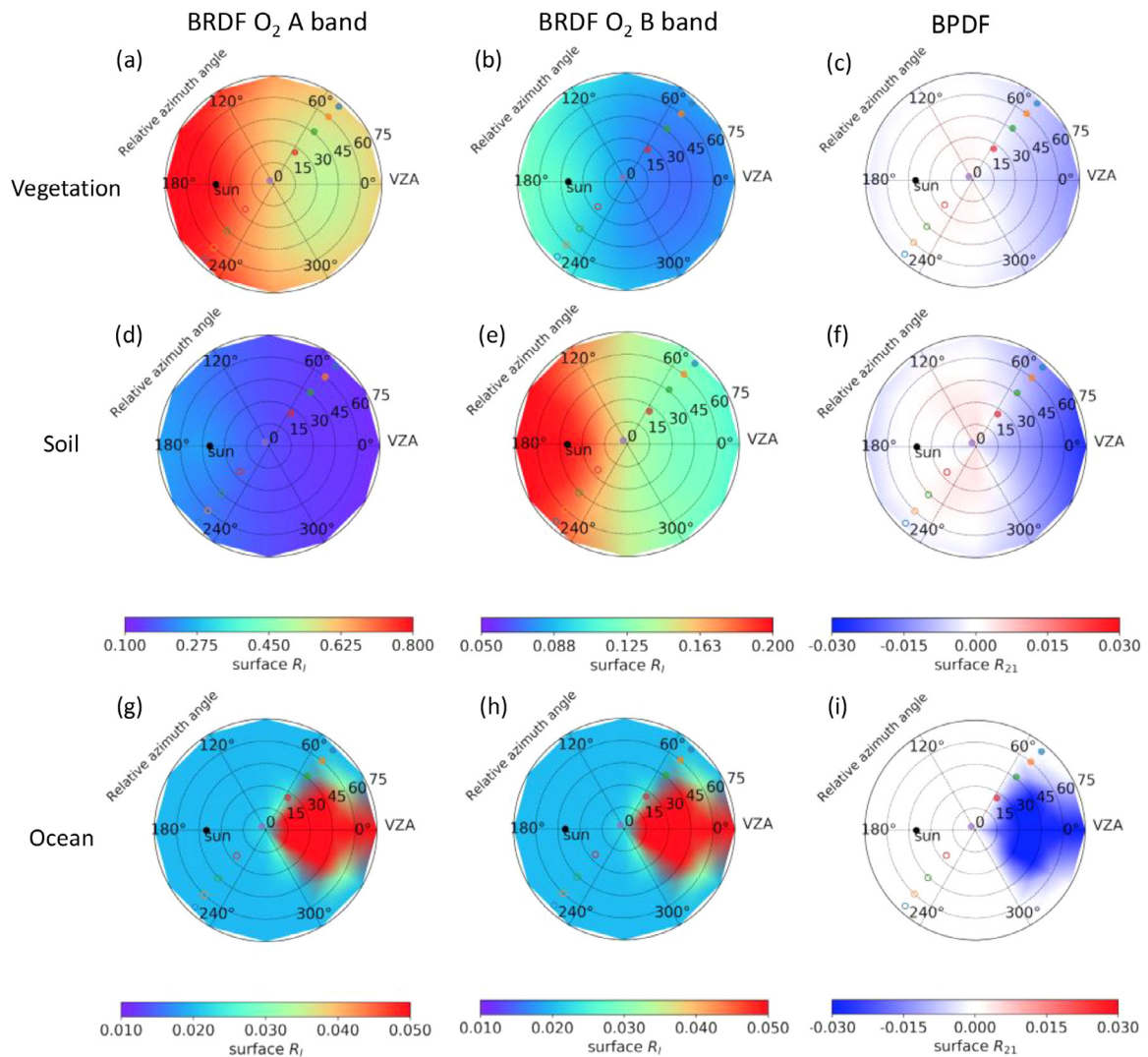


Fig. 3. Polar plots of R_{11} (BRDF) and R_{21} (BPDF) in surface reflectance matrix \mathbf{R} as expressed in Eq. (12) for vegetation (a-c), soil (d-f) and ocean (g-i) in O_2 A and B band. In each panel, the polar radius represents the viewing zenith angle (VZA) from 0° to 75° and the polar angle indicates the relative azimuth angle from 0° to 360° . The solar zenith angle (SZA) is fixed at 40° for all cases. The nine viewing angles are sampled in each panel using the same symbols as Fig. 2a. a), d) and g) are R_{11} in O_2 A band while b), d) and h) are R_{11} in O_2 B band. c), f) and i) show R_{21} for three surface types.

ometries should be taken into consideration due to the “step-to-stare” observation mode for single camera on MAIA. As an example, based on the assumption that the correlation decreases from the closest to the farthest pair of angles, the correlation coefficients between the angle Da and other angles are defined from 1.0 to 0.0 for angle Da to angle Df with an equal reduction of 1/8. Moreover, the observation accuracy of MAIA DOLP is decided by a polarization modulation technique enabled by a pair of photoelastic modulators and a pair of achromatic quarter-wave plates [8,9] and independent of light intensity detection. Hence, the radiance and DOLP measurement uncertainties at the same viewing geometries or in O_2 A and B band are still assumed independent. As a consequence, the correlation coefficient matrix (\mathbf{C}) is defined as shown in Fig. A1 (Appendix), so $\mathbf{S}_y = \mathbf{C} \times \mathbf{S}_{y0}$, where \mathbf{S}_{y0} is an error covariance matrix whose the i th row j th column element is the product of uncertainty of the i th and j th measurement ($\varepsilon_i \times \varepsilon_j$).

Because only two ALH parameters are involved in the state vector, other aerosol and surface parameters (such as AOD, SSA, and surface BRDF/BPDF parameters) in the forward model needs to be prescribed. In the case of MAIA, those parameters can be obtained from the MAIA aerosol and surface products. However, it is inevitable that uncertainties from those parameters may influ-

ence the forward simulation of observation and subsequently affect the ALH retrieval. Therefore, our observation error covariance matrix takes into account the modelling uncertainty as incurred from the uncertainties of those prescribed parameters. Based on around 15% expected uncertainty of AOD retrieval over land from MODIS [23], the uncertainty of AOD is assumed as 10% in all cases, while the impact of different AOD uncertainties on ALH retrieval uncertainty is assessed in the last part of Section 5. Similarly, the uncertainties of SSA and the linear combination coefficients of surface BRDF/BPDF kernels are assumed 3% and 10% in the analysis, respectively. Here, only the uncertainties of semi-empirical coefficients of three BRDF kernels and α in BPDF kernel, rather than other parameters in surface model are taken into consideration, whose Jacobians could be derived from UNL-VRM. Combining the diagonal error covariance matrix of \mathbf{b} (\mathbf{S}_b) with the Jacobians of these parameters (\mathbf{K}_b), the forward model parameter error covariance matrix (\mathbf{S}_m) can be derived from Eq. (4).

3.3. Experiment scenarios

Based on the instrument characteristics and simulation assumptions we mentioned above, the radiances and DOLP in both O_2 A

and B bands at nine angles are simulated by UNL-VRM. To compare the role of multi-angle or polarized measurements in each band on ALH retrieval, six scenarios including multi-angle measurements are defined in this study as shown in Table 3. The scenario A-I (or B-I) only includes radiance in O₂ A band (or O₂ B band), while A-IP (or B-IP) indicates both radiance and DOLP measurements in O₂ A band (or O₂ B band). Similarly, the scenario AB-I includes radiances in O₂ A and B band, and all measurements in two absorption bands are involved in scenario AB-IP. Hence, the scenario A-I and AB-IP represent the possible observations from MAIA and MAPMO, respectively. For each scenario, the DFS and posterior uncertainty of ALH are calculated when the number of viewing angles increases from one to nine.

In the following analysis, we first analyze the information contained in total measurements of MAIA and MAPMO, i.e. scenario A-I and AB-IP, in section 4. Next, the effect of each type of measurements, e.g. multi-angle, DOLP or O₂ B measurements, is extracted by comparing the ALH posterior uncertainties for different scenarios in section 5. For instance, the impact of polarized measurements in O₂ A band could be summarized by comparing the retrieval uncertainty between scenario A-I and A-IP. Similarly, the impact of radiance measurements in O₂ B band could be derived from the difference between scenario A-I and AB-I.

4. Information from MAIA and MAPMO observations

Firstly, to quantify the ALH information, not only the TOA radiance and DOLP, but also their Jacobians with respect to ALH parameters are simulated from UNL-VRM, expressed as $\frac{\partial I_a}{\partial H_{\text{peak}}}$ and $\frac{\partial \text{DOLP}_a}{\partial H_{\text{peak}}}$ in Fig. 4. The Jacobian represents the sensitivity of each measurement (I_a or DOLP_a) to each retrieved parameter. After applying these simulations for MAIA and MAPMO in Eq. (5), the averaging kernel matrix **A** for two retrieved parameters H_{peak} and w of ALH are derived. The two diagonal elements in **A** represent the DFS of H_{peak} and w , whose value range from 0 to 1.0. For a given parameter, the closer DFS is to 1.0, the greater the information content provided by the observations. The DFS of ALH parameters from observations of MAIA and MAPMO (scenario A-I and AB-IP in Table 3) are summarized in subsection 4.1 and compared for difference surface and aerosol types with several AOD. The AOD values in this paper are all for 749 nm (O₂ A continuum band). In subsection 4.2, we analysed how H_{peak} and w DFS change when different numbers of viewing geometries are involved in the measurement vector.

4.1. Different surface and aerosol types

Compared with MAIA, MAPMO includes additional polarization in O₂ A band and both radiance and polarization in O₂ B band. Each DFS of two ALH parameters, H_{peak} and w , from MAIA and MAPMO nine-angle measurements over three different types of surface for both BB and UI aerosols for 3 km H_{peak} is summarized in Table 4. It is found that both MAIA and MAPMO measurements have high information content for H_{peak} , regardless of aerosol and surface type, as DFS is always larger than 0.8. However, over vegetation, DFS of H_{peak} shows 0.03–0.07 lower than the other two surface types for MAIA. The reason is that radiance Jacobians in O₂ A band is lower for vegetation surface than ocean and soil for 3 km H_{peak} , indicating less sensitive to ALH, although the difference of radiance Jacobians between three surface types is not as much as DOLP Jacobians (Fig. 4c and Fig. 4g). In O₂ B band, DOLP sensitivity over vegetation is not the lowest, but this improvement only reduces the DFS difference between vegetation and other two surfaces for MAPMO. Anyway, even though MAPMO involves O₂ B band measurements compared with MAIA, the ALH DFS is still

Table 4

DFS of H_{peak} and w from MAIA and MAPMO measurements at all nine angles over ocean, soil and vegetation surface when AOD is 1.5 at 749 nm for a profile with 3 km H_{peak} and 1 km width.

Surface and aerosol type	H_{peak}	w	
ocean	Biomass burning (BB)	0.92/0.97 ^a	0.53/0.82
	Urban industrial (UI)	0.91/0.96	0.34/0.72
vegetation	Biomass burning (BB)	0.88/0.94	0.29/0.72
	Urban industrial (UI)	0.84/0.92	0.15/0.55
soil	Biomass burning (BB)	0.92/0.96	0.50/0.82
	Urban industrial (UI)	0.91/0.95	0.32/0.70

^a : The left values separated by symbol “/” are for MAIA and the right values are for MAPMO measurements.

the lowest over vegetation. Due to additional DOLP in O₂ A band and all measurements in O₂ B band, MAPMO contains 0.04–0.07 more DFS than MAIA. Moreover, the difference of both radiance and DOLP sensitivities between two aerosol types varies significantly when AOD and viewing geometries change (Fig. 4b and 4f), causing inconsistent DFS differences between BB and UI. For example, at large AOD (AOD = 1.5), BB has 0.01–0.02 larger DFS than UI from MAIA and MAPMO measurements no matter the surface type (Table 4). Generally, the surface reflectance has more impact on the information content of H_{peak} from MAPMO and MAIA measurements than aerosol optical properties, leading to the lowest information content over vegetation.

Compared with H_{peak} , less information about w is obtained from MAIA (or MAPMO) based on its lower DFS (0.1–0.4 for MAIA and 0.5–0.8 for MAPMO) (Table 4), resulting from less sensitivity of radiance to w (Fig. 4d). In contrast, the sensitivity of DOLP to w is larger than that of H_{peak} (Fig. 4h) at several specific viewing angles, resulting in the more information of w contained in MAPMO than MAIA. In fact, similar to H_{peak} , observations over vegetation contain the lowest information of w with lower 0.15 to 0.25 (0.1 to 0.2) DFS than ocean and soil for MAIA (MAPMO). Between the two aerosol types, the w DFS of BB is larger than that of UI, whose difference could reach 0.2 over vegetation, indicating a better performance of MAPMO and MAIA observations in ALH retrievals for absorbing aerosols. In general, different surface reflectance and aerosol optical properties have a greater influence on w information than H_{peak} for MAIA and MAPMO measurements.

Besides BB and UI we discussed above, the mineral dust is also an important type of aerosols with less absorbing than BB but more scattering. The simulation in O₂ A and/or B band for dust particles has been conducted in our previous studies [10,40], as well as the ALH information, which were not discussed in detail here. Generally, it has been found that the less absorbing dust particles would improve the multiple scattering in the atmosphere, which is suppressed by highly absorbing aerosols (such as BB). As a result, the DOLP in O₂ absorption band is more sensitive to moderately absorbing dust particles, indicating larger information [10]. Furthermore, sometimes dust particles present non-spherical and the impact of dust particle shape on the DOLP in O₂ absorption band has been analyzed in [40]. The DOLP at TOA depends more on positive Rayleigh scattering DOLP if more O₂ absorption happens due to lower aerosol altitude (and less on aerosol scattering). Compared with spheres, the DOLP of spheroids is smaller, especially close to backscattering, revealing less sensitivity of TOA DOLP to H_{peak} . Moreover, while these differences of DFS exist between various type of aerosols because of their different single scattering optical properties, the dependence of DFS on surface types and the impact of multi-angle and/or polarized measurements generally appear similar. While we have tackled the impact of dust particle shape to some degree in previous study, dealing with dust non-sphericity shape deserves more future work.

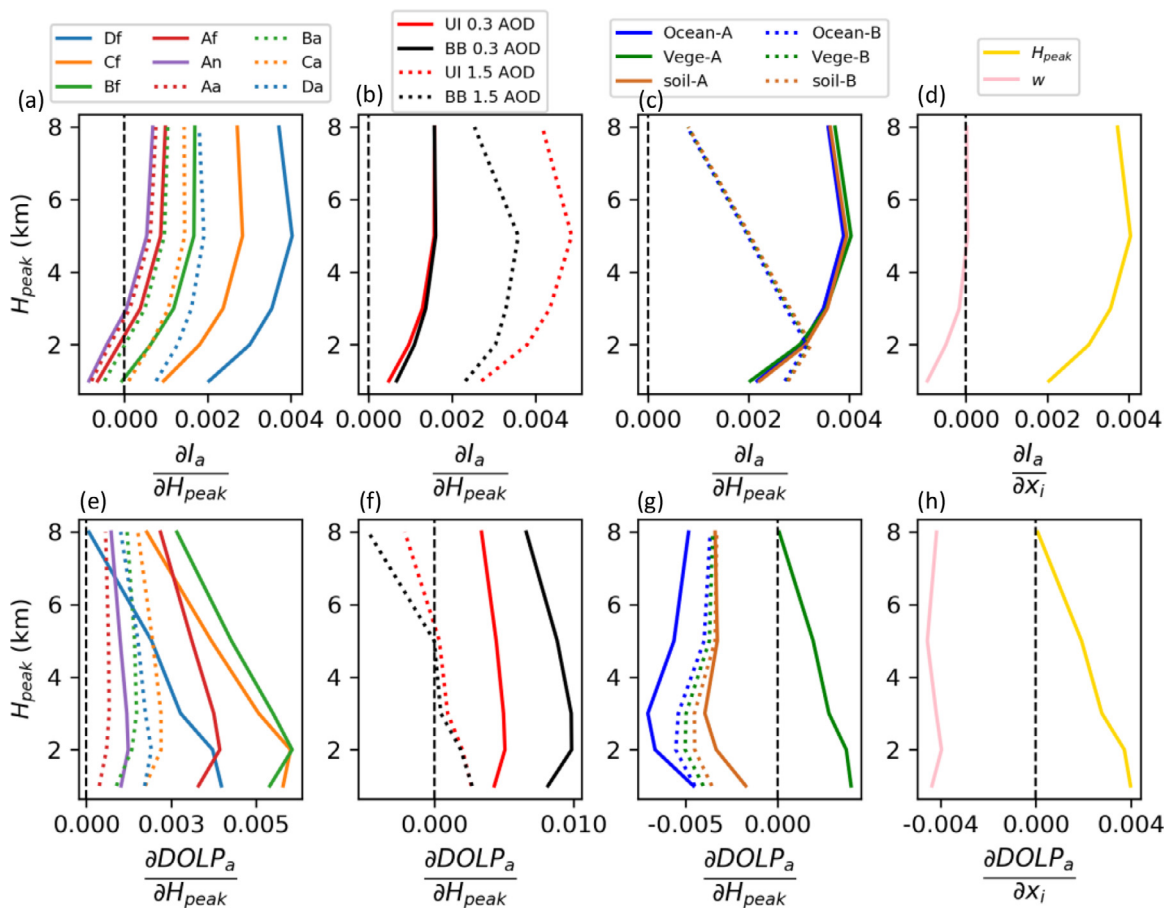


Fig. 4. The variation of Jacobians of radiance (I_a , the first row) and DOLP ($DOLP_a$, the second row) in O_2 absorption bands with respect to H_{peak} as a function of H_{peak} . a) and e) show UI aerosol Jacobians in O_2 A band at nine viewing geometries defined in Fig. 2a over vegetation surface with 1.0 AOD. b) and f) indicate Jacobians in O_2 A band with Df viewing geometry over vegetation at two AOD for two aerosol types. The Jacobians to H_{peak} in O_2 A and B band are compared in c) and g) over different surface types, keeping 1.0 AOD and Df viewing geometry for UI aerosol. d) and h) show the comparison of Jacobians to H_{peak} and w over vegetation with the same AOD, viewing geometry and aerosol type as c). The black dash lines show zero value. The value of w is fixed at 1 km for all cases.

4.2. Different number of view angles

Consistent with our previous studies [10,40], the sensitivity of TOA radiance to H_{peak} decreases at lower aerosol layer, since the stronger Rayleigh scattering supplements the radiation absorbed by more O_2 concentration, leading to less TOA radiance reduction with the same H_{peak} change. Similarly, the TOA DOLP is more sensitive to lower H_{peak} (Fig. 4a and 4e), due to the stronger Rayleigh scattering DOLP as well. In fact, both the Rayleigh scattering and aerosol scattering depend on the scattering angle, determined by solar geometry and viewing geometry (Fig. 2b and 2c). Thus, the sensitivity of TOA measurement to H_{peak} varies with different viewing angles (Fig. 4a and 4e). For instance, if the aerosol scattering phase function at one viewing angle is stronger (Df) and closer to Rayleigh scattering, the change of relative weights between Rayleigh scattering and aerosol scattering due to the variation of H_{peak} will cause less total scattering change and TOA radiance mainly depends on O_2 absorption change. Thus, TOA radiance is more sensitive. When gathering measurements from multiple viewing geometries focusing on the same target, the number of angles should be decided to obtain enough information for the state vector retrieval. Therefore, we analyzed the dependence of the information about ALH parameters on the number of viewing angles contained in the multi-angle retrieval. When observations at more than one viewing angle are involved in the retrieval, angles are selected following the sensitivity of radiance to H_{peak} quantified by its Jacobian from the highest to the lowest. As shown in Fig. 4a, the

sensitivities at nine angles are sorted from the largest to the lowest as: Df, Cf, Da, Bf, Ca, Ba, Af, Aa, An. In other words, when retrieving ALH using 3-angle measurements, the first three angles (Df, Cf, Da) showing the strongest sensitivity are used. This sequence remains consistent in all scenarios although the radiance sensitivity at different angles depends on aerosol type, AOD, and H_{peak} . By this method, the DFS about H_{peak} and w when MAPMO observations at one to nine angles included in the retrieval are compared with those from MAIA measurements in Fig. 5. Given the dependence of radiance and DOLP Jacobians on AOD (Fig. 4b and 4f), the DFS at two AOD (0.3 and 1.5) are compared in Fig. 5 as well.

Firstly, the change of H_{peak} DFS with the number of viewing angles used in the retrieval is analysed. As we discussed in Section 4.1, the DFS of H_{peak} from either MAPMO or MAIA nine-angle measurements is the highest over ocean, and next over soil, while the lowest over vegetation. However, when the number of angles used in the retrieval increases from one to nine, H_{peak} DFS increases most over vegetation with 0.1–0.25 DFS increment (Fig. 5b). Over both soil and ocean, the DFS increment does not exceed 0.1. This is because the sensitivity of observations to ALH is not so distinct at different viewing geometries for low surface reflectance. On the other hand, we also pay attention to the minimum viewing angles satisfying high information of ALH. In the real multi-angle observation mode of MAIA, if more angles stare at one Earth target, the spatial coverage or the total number of targets for MAIA will be reduced considering limited observation time. This is why an optimal number of angles has to be found

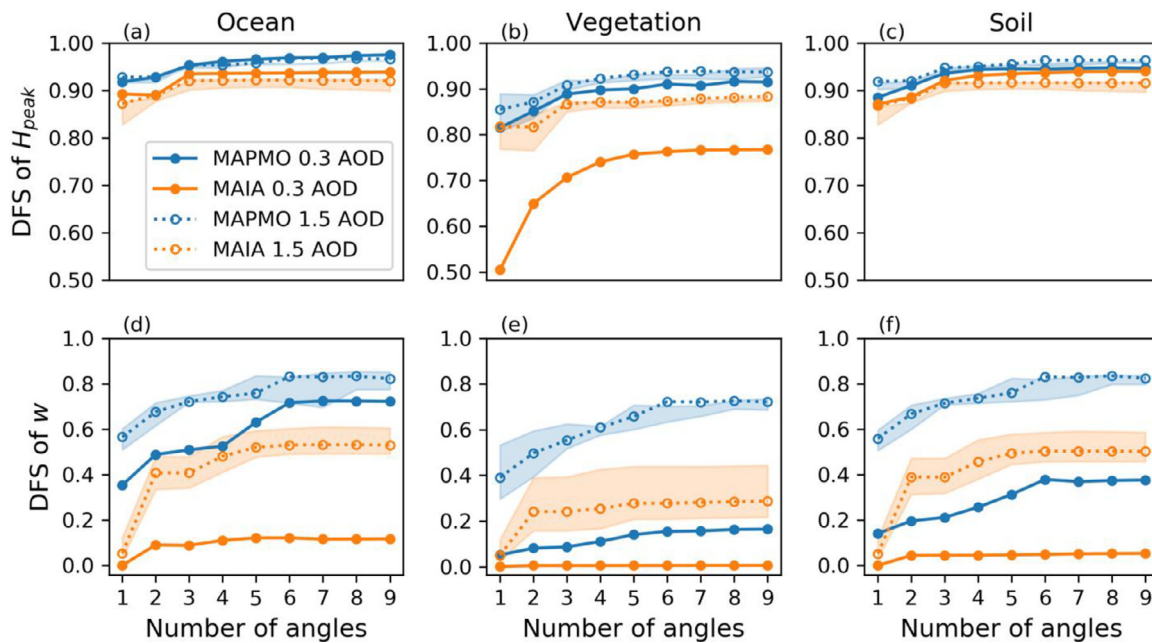


Fig. 5. DFS of H_{peak} (a-c) and w (d-f) for BB aerosol from multi-angle measurements of MAIA (orange lines) and multi-angle polarimetric measurements at two O_2 bands of MAPMO (blue lines) when different numbers of viewing geometries are included. The left (a and d), middle (b and e) and right columns (c and f) are over ocean, vegetation and soil surface, respectively. The solid scatter lines are for 0.3 AOD and dotted scatter lines are for 1.5 AOD. The aerosol profile is defined as 3 km H_{peak} and 1 km w . The blue and orange shades represent the DFS range when SZA varies from 25° to 60° for MAPMO and MAIA at 1.5 AOD, respectively. While solar geometries change, other scenario configurations keep the same.

to keep high ALH information while reduce observation time per target for different scenarios. From Fig. 5, when the number of observation angles reaches six, adding more measurements at other angles will increase DFS little, while the largest increment happens when increasing from a single angle to two or three angles. Thus, six angles are optimal for multi-angle satellite ALH retrieval. Secondly, we'd like to look at the impact of AOD on multi-angle ALH retrieval. Over ocean and soil (Fig. 5a and 5c), different AOD causes little difference not only in the dependence of H_{peak} DFS on the number of angles used, but also the DFS value itself, for both MAIA and MAPMO measurements. In contrast, over vegetation, the DFS difference caused by different AOD could be 0.05 for MAPMO observations, and even more than 0.1 for MAIA (Fig. 5b), due to the larger difference in the sensitivity over vegetation between different AOD. Furthermore, the impact of solar geometry on the ALH DFS is analyzed. Lines in Fig. 5 represent the DFS at 40° SZA, while the shaded areas show the DFS ranges when SZA changes from 25° over 60° (corresponding SAZ values are given in Fig. 2a). In total, different light path length resulting from various SZA causes less than 0.1 DFS difference. For multi-angle measurements, this light path impact is stronger on MAIA measurements than MAPMO. Compared with multi-angle measurements, solar geometries affect H_{peak} DFS from single-angle measurements more. Last but not least, comparing MAIA and MAPMO observations, at small AOD over vegetation, the DFS difference between these two scenarios is reduced from 0.4 to 0.15 when adding more angles. However, if AOD is large, both MAPMO and MAIA contain large H_{peak} DFS (> 0.8) even for single-angle measurements, resulting in consistent 0.07 DFS difference regardless of how many angles are used. Unlike vegetation, the DFS difference between MAPMO and MAIA is less than 0.05 over ocean and soil, independent of AOD and the number of angles used. In other words, the number of angles and AOD affect H_{peak} information from MAIA and MAPMO over vegetation rather than ocean and soil.

The DFS of w is much less than H_{peak} for the same scenarios, but the increase in DFS due to adding angles can exceed 0.4, much more than occurs for H_{peak} , which illustrates the major improvement in w retrieval when using multi-angle measurements (Fig. 5d–5f). Unfortunately, for MAIA, if AOD is small, using more measurements at different angles cannot improve w information effectively, and DFS remains less than 0.1. Greater improvement is found at larger AOD. This conclusion about AOD dependence of multi-angle improvement of w DFS is also applied for MAPMO over vegetation (blue lines in Fig. 5e). In contrast, this DFS increasing due to multi-angle measurements are similar at different AOD over ocean and soil (blue lines in Fig. 5d and 5f). However, unlike H_{peak} , AOD affects not only the multi-angle improvement of w DFS, but also the DFS value itself. For instance, MAPMO observations provide 0.1–0.2 more w DFS over ocean and 0.4 more over soil at larger AOD. Given the lower DFS of w than H_{peak} , light path (or SZA) has larger impact on the information for w , such as more than 0.2 DFS difference can be found over vegetation. Similar to H_{peak} , the w DFS from MAIA multi-angle measurements depends more on SZA than single-angle measurements, indicating the longer light path cannot increase w DFS from single-angle measurements due to its low information. On the contrary, the w DFS contained in MAPMO single-angle and multi-angle measurements have similar dependence on SZA since the polarization sensitivity is less affected by the light path length. In Fig. 5, we only show the results for BB aerosol. The UI aerosol presents similar patterns but with smaller values of DFS, so are not shown here.

In summary, although multi-angle measurements provide more information to retrieve ALH, especially for parameter w , ALH information increases little when more than six angles are involved in the retrieval for both MAIA and MAPMO. The lowest information content is provided over vegetation, meanwhile multi-angle measurements improve H_{peak} information the most. In addition, the number of angles and AOD affect w information a lot, but only influence H_{peak} information over vegetation.

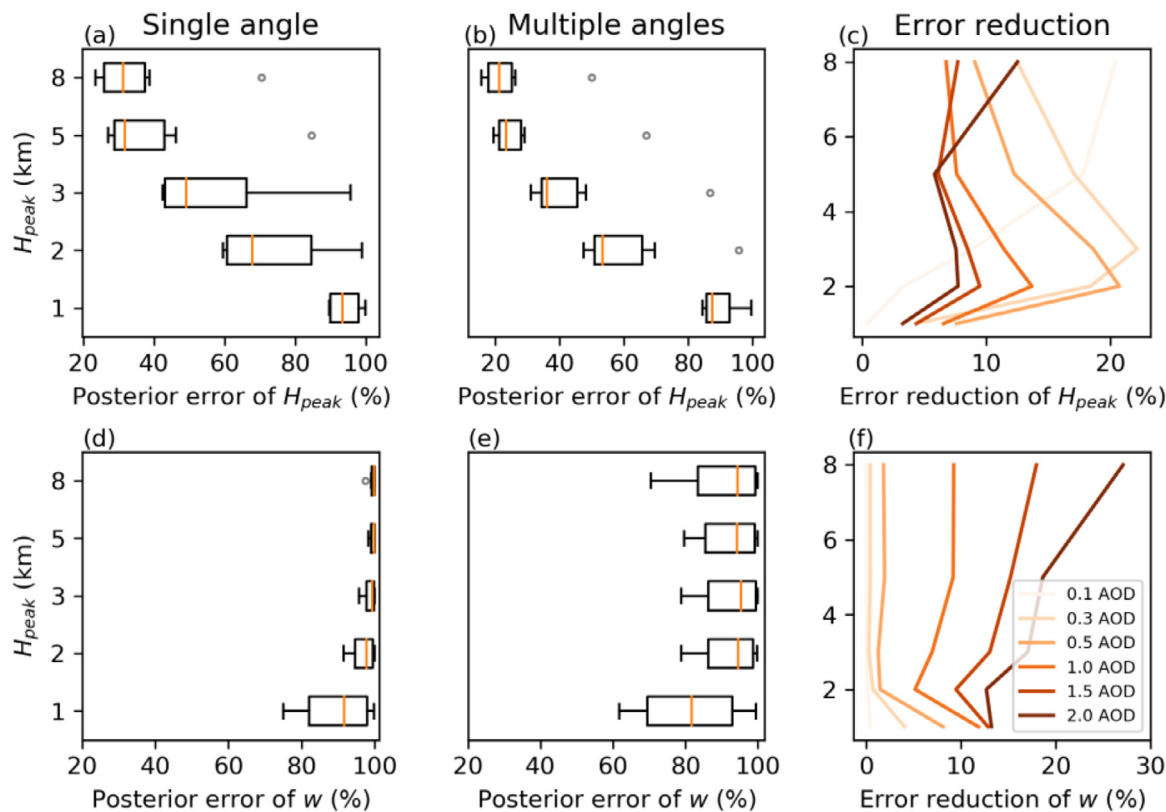


Fig. 6. The posterior uncertainty of H_{peak} (first row) and w (second row) for single-angle measurements (a and d) and multi-angle measurements (b and e) in O_2 A band, as well as the uncertainty reduction between these two types of measurements. Each box in the panel a, b, d and e represents the statistics of posterior uncertainties for AOD from 0.1 to 2.0. The six AOD points in each box are the same as different lines shown in panel (c) and (f). On each box, the central mark indicates the median, and the left and right edges of the box indicate the 25th (q_1) and 75th (q_3) percentiles, respectively. The whiskers extend from $q_3 + 1.5 \times (q_3 - q_1)$ to $q_1 - 1.5 \times (q_3 - q_1)$, and the data exceeding this range are plotted as outliers using the circle symbol. For single-angle measurements, we select the angle D_f , while multi-angle indicates nine-angle measurements. Both the uncertainty reduction and posterior uncertainty are shown as the percentage of the true value. Here we do not add polarimetric measurements for both single and multiple angles. In these cases, the w is assumed 1 km and the surface is vegetation.

5. The role of multi-angle and polarimetric measurements

The potential capability of a hypothetical MAPMO instrument and MAIA to retrieve ALH parameters were analysed in Section 4. Realization of a practical instrument design requires an analysis of the trade-offs between multi-angle, polarization, and O_2 B band measurements in retrieval of ALH. In this section, we explore these trade-offs and try to figure out the role of each kind of measurements by comparing the retrieval uncertainties in different scenarios in Table 3. Furthermore, each component in the retrieval uncertainty is compared between different scenarios as well. We describe the posterior uncertainty as a percentage of true value for each parameter in the state vector (H_{peak} and w), the same to the prior uncertainty assumed as 100% for all cases as discussed in Section 3.2.2.

5.1. The improvement of multi-angle measurements

In this section, we first compare the ALH retrieval uncertainty from single-angle measurement and nine-angle measurements (Fig. 6). Then, the uncertainty reduction of multi-angle retrieval when viewing angle increases from one to nine is analysed (Fig. 7). To answer question (a) in Section 1, the posterior uncertainties of H_{peak} and w in scenario A-I at one vs. nine angles are summarized in Fig. 6 (a, b, d and e). Each box indicates the uncertainty range when AOD is from 0.1 to 2.0. Considering the same prior uncertainty, a smaller posterior uncertainty corresponds to larger information content of the observations. From both single-angle and multi-angle measurements, the posterior uncertainty of

H_{peak} decreases when AOD and H_{peak} increase, whereas the uncertainty distribution at different AOD shows significant distinction (Fig. 6a and 6b). For single-angle observation, when H_{peak} is lower than 3 km, although the mean posterior uncertainty of different AOD decreases at higher H_{peak} , the range of posterior uncertainty increases. This implies at small AOD, the H_{peak} information from single-angle measurement is low in the boundary layer, but the information increases significantly when AOD is larger, especially for 2–3 km H_{peak} . For the multi-angle, the ranges of posterior uncertainty change little when H_{peak} varies, except for 0.1 AOD (represented by outliers in Fig. 6b), indicating the similar impact of AOD on H_{peak} retrieval at different H_{peak} . At each H_{peak} , the H_{peak} uncertainty range in multi-angle retrieval is smaller than that in single-angle retrieval, illustrating the less impact of AOD in multi-angle H_{peak} retrieval. The situation is different for parameter w . At lower H_{peak} in single-angle retrieval, the w uncertainty is smaller at larger AOD, but keeps large at all AOD for higher H_{peak} , demonstrating the larger impact of AOD on w retrieval near the surface (Fig. 6d). For the multi-angle retrieval, the w posterior uncertainty shows similar variation with H_{peak} increasing as single-angle retrieval, but the impact of AOD on w information is magnified by multi-angle measurements, especially at higher H_{peak} .

To quantify the retrieval uncertainty reduced by multi-angle measurements compared with single-angle measurement, the right column in Fig. 6 (Fig. 6c and 6f) shows the uncertainty difference between the left and middle columns. For H_{peak} , multi-angle measurements reduce retrieval uncertainty more for smaller AOD, by as much as 20%, indicating that the benefit of multi-angle measurements for ALH retrieval decreases as AOD increases (Fig. 6c).

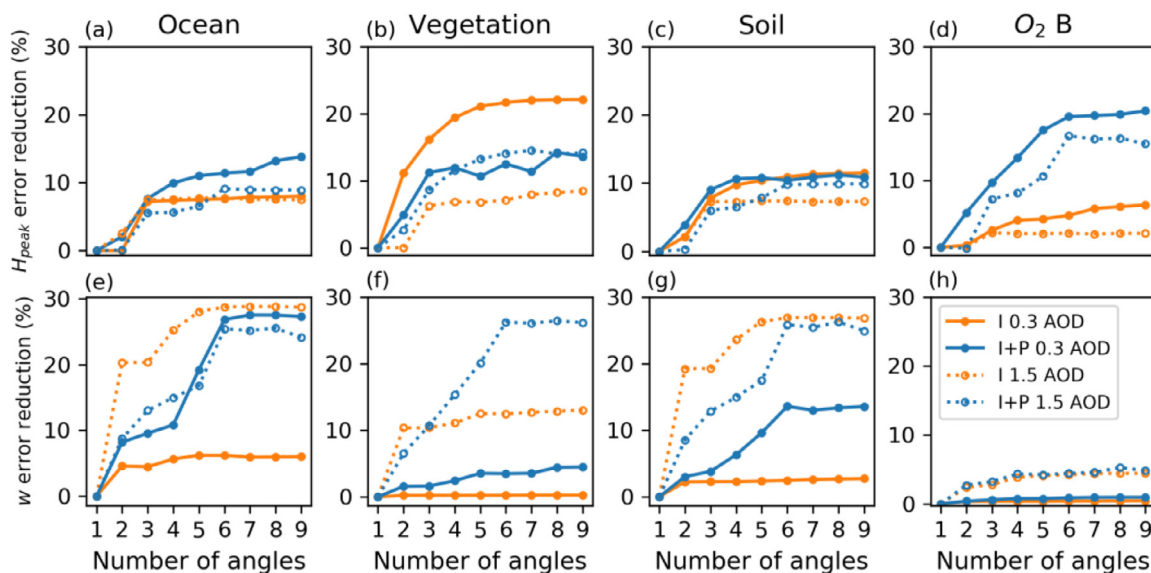


Fig. 7. The variation of uncertainty reduction expressed as a percentage between single-angle and multi-angle measurements for H_{peak} (the first row) and w (the second row) with the number of angles used in the retrieval for BB aerosol with or without polarized measurements. The first three columns are for ocean, vegetation and soil surface in O_2 A band, while the last column shows results over vegetation in O_2 B band. The green lines show radiance-only retrieval, and the red lines indicate retrievals from both radiance and DOLP measurements. The solid scatter lines and dotted scatter lines represent 0.3 and 1.5 AOD, respectively. The other parameters are the same as Fig. 5.

The reason is that when AOD is large, the single-angle measurements already provide large H_{peak} information; if adding more angles, the H_{peak} information is improved a little bit, but much smaller than lower AOD having little H_{peak} information at single angle. For different H_{peak} , multi-angle retrieval reduces the H_{peak} uncertainty most at 2–3 km H_{peak} except too small AOD. On the other hand, for w , the uncertainty reduction due to multi-angle measurements is large for near surface H_{peak} and increases as AOD increases. At higher H_{peak} , this uncertainty reduction is low at small AOD but increases at larger AOD, and can reach 30% when AOD is 2.0 (Fig. 6f).

Additionally, the dependence of this uncertainty reduction from multi-angle measurements on the number of viewing angles is presented in Fig. 7 for scenario A-I, A-IP, B-I and B-IP. Two AOD and three surface types are compared. For H_{peak} , although the uncertainty reduction increases when the number of angles increases, a threshold is reached when six or more angles are involved in the retrieval (Fig. 7a–7d). Comparing scenario A-I over three types of surface (Fig. 7a–7c), the H_{peak} uncertainty is reduced more than 20% due to multi-angle measurements over vegetation at small AOD, but only around 10% over ocean and soil, or over vegetation at large AOD, showing the essential role of multi-angle measurements for vegetated surfaces at smaller AOD. However, the multi-angle uncertainty reduction for scenario A-IP depends less on surface type, and is around 15%, similar or smaller than for A-I cases. This uncertainty reduction shows little dependence on AOD, neither, but over ocean, the AOD impact is larger than that in scenario A-I. For scenarios B-I and B-IP, there is less distinction between different surface types, hence only the uncertainty reduction over vegetation is shown in Fig. 7d. Unlike scenario A-IP, the multi-angle measurements in O_2 B band improve the posterior uncertainty by up to 20% when polarized measurements are included (scenario B-IP). However, for B-I cases, multiple angles improve the retrieval less in the O_2 B band than in the O_2 A band, regardless of AOD. In O_2 B band, the improvement of multi-angle measurements is stronger at lower AOD, and this dependence on AOD is similar for B-I and B-IP cases.

Focusing on parameter w , multi-angle measurements in the O_2 A band improve its retrieval more over ocean and soil, especially

for A-I cases, the opposite of what is observed for the parameter H_{peak} . This uncertainty reduction improves as AOD increases, and the multi-angle improvement for scenario A-IP is greater than A-I at small AOD for all surface types. On the contrary, at large AOD, the multi-angle measurements improve A-I retrieval more than A-IP over ocean and soil. In the O_2 B band, the multi-angle measurement improves w retrieval much less than O_2 A band, with or without polarization. Higher AOD yields greater improvement in O_2 B band, but is still below 5%. All the cases in Fig. 7 are for BB aerosol, while the uncertainty reductions for UI aerosol are shown in Appendix (Fig. A3).

In conclusion, compared with single-angle radiance-only measurements, multi-angle measurements in O_2 A band improve H_{peak} retrieval more over vegetation surface at smaller AOD, and reduce w retrieval uncertainty more at larger AOD over ocean and soil. Including polarization, multi-angle measurements improve single-angle H_{peak} retrieval equally or greater than radiance-only measurements, except over vegetation at small AOD in O_2 A band. Generally, the multi-angle measurements improve w retrieval more than H_{peak} , but less at small AOD over vegetation and in O_2 B band.

5.2. The improvement of adding polarization measurements

Fig. 8 compares the posterior uncertainties of H_{peak} and w for scenarios A-I and A-IP and addresses how much uncertainty reduction would be improved by adding polarization to MAIA-like multi-angle O_2 A band measurements. For H_{peak} , each box in Fig. 8a–8c represents the statistics of the posterior uncertainty or uncertainty reduction when the number of angles in the retrieval increases from one to nine. It is found that the posterior uncertainty of H_{peak} for A-I and A-IP case decreases dramatically from 90% to around 20% with increasing H_{peak} , indicating more H_{peak} information contained in middle troposphere (Fig. 8a and 8b). Among the three surface types considered, the posterior uncertainty of H_{peak} is the highest over vegetation while adding DOLP and multi-angle measurements cannot change the situation. However, for scenario A-IP, changing the number of angles causes larger uncertainty difference over ocean and soil compared with scenario A-I, especially for lower H_{peak} , reaching 10%–15% (Fig. 8b). From Fig. 8c, it is clear

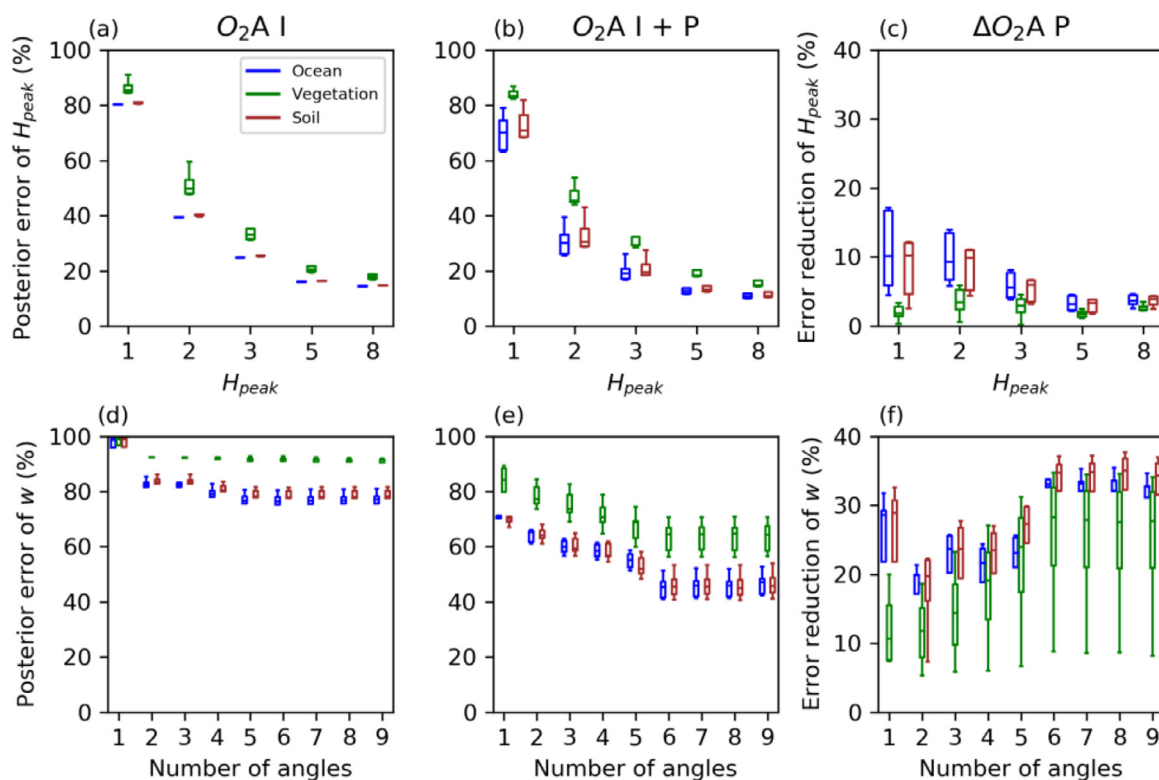


Fig. 8. The posterior uncertainties of H_{peak} and w from multi-angle radiance measurements (a and d) and adding DOLP measurements (b and e), as well as the uncertainty reduction between these two types measurements (c and f). Only O_2 A band is used for all cases. Each box of H_{peak} uncertainty (a-c) represents its statistics for the number of angles used from 1 to 9 at different H_{peak} , while w uncertainty box is for H_{peak} from 1 to 8 km at each number of angles (d-f). In scenario A-I and A-IP, each box of the w posterior uncertainty represents the lowest value at 1 km H_{peak} but similar values at other heights. Only over vegetation in panel (f), the uncertainty reduction increases when H_{peak} increases. The marker and whisker of each box represents similar statistical variables as in Fig. 6 except using vertical box instead of horizontal box here. Different box colors show three surface types. All cases here are for BB when AOD is 1.0 at 749 nm and w is 1 km.

that the H_{peak} retrieval uncertainty could be reduced 5%-18% due to adding polarized measurements. This uncertainty reduction increases as H_{peak} decreases over ocean and soil, while changes little with H_{peak} over vegetation. Generally, DOLP measurements improve the ALH retrieval more due to their larger sensitivity when aerosols are located at low altitudes (Fig. 4e). Compared with ocean and soil, the uncertainty reduction due to DOLP over vegetation is lower (< 5%). Moreover, when a different number of angles are added, the uncertainty reduction could be changed as much as 13% over ocean at 1 km H_{peak} .

For parameter w , its posterior uncertainty is found to have little dependence on H_{peak} (except shows lower values at 1 km H_{peak}), hence only the uncertainty or uncertainty reduction range at different H_{peak} is shown in each box. The posterior uncertainty of w is always larger than 80% even for multi-angle measurements of scenario A-I (Fig. 8d). Neither increasing the number of angles used in the retrieval nor changing H_{peak} would reduce the posterior uncertainty due to the small sensitivity of radiance to w (Fig. 4d). In contrast, the number of angles has effect on w posterior uncertainty and different H_{peak} could also cause 5%-10% posterior uncertainty difference for scenario A-IP (Fig. 8e). Furthermore, the uncertainty reduction due to adding multi-angle DOLP in O_2 A band ranges from 5% to more than 35% and shows significant dependence on the number of angles and H_{peak} (Fig. 8f). Over soil and ocean, DOLP measurements improve the single-angle retrieval significantly, but improve less when two to five angles used in the retrieval. Over vegetation, the uncertainty reduction due to DOLP increases when adding more angles. One the other hand, the uncertainty reduction from DOLP increases 10%-20% as H_{peak} increases over vegetation, but only 5%-10% over ocean and soil.

Similar to the study in [10], DOLP measurements improve the sensitive to H_{peak} for lower aerosol layer. In conclusion, adding DOLP measurements improves w retrieval uncertainty more than H_{peak} . Among different surface types, the ALH retrieval over vegetation surface is improved less compared to soil and ocean. The posterior uncertainty of H_{peak} is reduced more at lower H_{peak} due to DOLP but the opposite is true for w . Given the less variation of w value than H_{peak} in reality, the dependence of ALH posterior uncertainties are analysed in the Appendix instead of main text here. The uncertainties of H_{peak} and w are reduced by DOLP more when more angles are used in the multi-angle retrieval.

5.3. The improvement of adding O_2 B band

In this part, we analyse the improvement in ALH retrieval from adding O_2 B measurements by comparing the scenarios A-I, AB-I and A-IP, AB-IP. The left column in Fig. 9 illustrates the uncertainty reduction by adding O_2 B radiance-only measurements (the difference between A-I and AB-I), and the right column shows the uncertainty reduction from O_2 B radiance and DOLP measurements (the difference between A-IP and AB-IP). In this figure, each box represents the range of uncertainty reduction as different number of angles are used in the retrieval. It is clear that no matter whether polarized measurements in O_2 B band are added or not, the retrievals of both H_{peak} and w over vegetation are improved by O_2 B measurements to a greater extent than the other two types of surface. This is due to the much lower surface albedo for vegetation in O_2 B band than A band, consistent with the conclusion about the O_2 B band's benefit in ALH retrieval over land from [35]. Moreover, when the number of angles involved in the retrieval increases from one to nine, the uncertainty reductions of

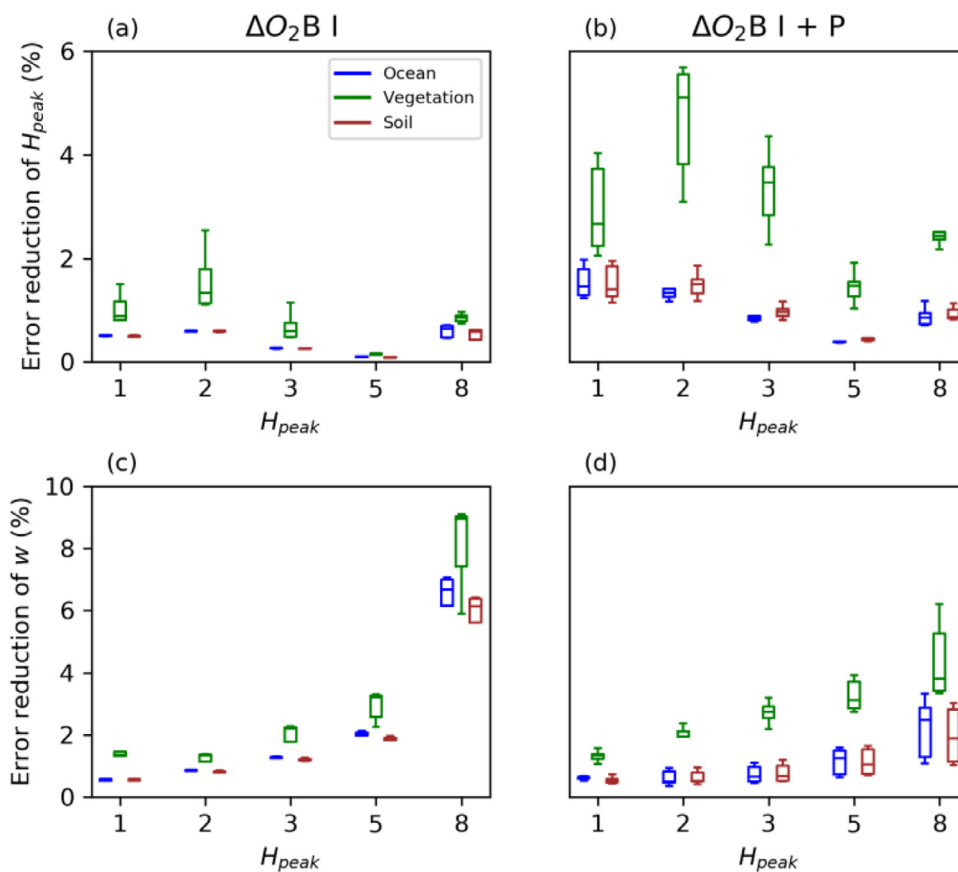


Fig. 9. The posterior uncertainty reduction of H_{peak} and w from adding radiance-only measurements (a and c) or both radiance and polarization of O_2 B band (b and d) measurements into O_2 A measurements. Each box represents the same statistics for different number of angles used as Fig. 8a, and all cases have the same parameters as well.

both parameters change less (smaller ranges of boxes) for ocean and soil than for vegetation surface, indicating the larger impact of the number of angles on O_2 B improvement over vegetation. This dependence on the number of angles of uncertainty reduction from adding radiance and DOLP in O_2 B band shows more than that from O_2 B radiance-only measurements, reaching 2.5% uncertainty reduction difference. For both H_{peak} and w , the change of uncertainty reductions with H_{peak} is independent of whether DOLP in O_2 B band is included or not.

The O_2 B observations affect the uncertainties in H_{peak} and w differently. Firstly, consider the variation of uncertainty reductions with H_{peak} . H_{peak} retrieval is improved the most at 1–2 km H_{peak} whose uncertainty reduction could be more than 2% due to adding radiance-only measurements in O_2 B band and 5% from adding both radiance and polarized measurements in O_2 B band, while the least improvement occurs at 5 km H_{peak} with only 0.1–0.5% uncertainty reduction (Fig. 9a and 9b). The previous study [35] also found similar result that the inclusion of O_2 B band radiance provides an increased sensitivity to atmospheric layers close to the surface. However, the uncertainty reduction of w increases at higher H_{peak} , reaching 10% from radiance-only measurements in O_2 B band (6% for both radiance and polarized measurements in O_2 B band) (Fig. 9c and 9d). These findings demonstrate that both radiance and DOLP measurements in O_2 B band improve the H_{peak} retrieval more when aerosols are concentrated at lower altitudes, but less for w retrieval at these altitudes. Furthermore, the comparison of improvement from radiance-only O_2 B measurements and from both radiance and DOLP measurements shows distinction for H_{peak} and w . For H_{peak} , when both radiance and DOLP in O_2 B are added (scenario AB-IP), the posterior uncertainties of

scenario A-IP are reduced 1–4% more compared with the uncertainty reduction between scenario AB-I and A-I (Fig. 9a and 9b). For w , the improvement from O_2 B radiance and DOLP measurements or radiance-only measurements is similar and even smaller at high H_{peak} (8 km). That is because unlike low w information in A-I measurements, the A-IP measurements have provided large w information and adding B-IP measurements could reduce the posterior uncertainty at some extent, but not as much as that comparing A-I and AB-I, similar to the findings in [4]. Therefore, DOLP in O_2 B band is more useful for H_{peak} than w . Generally speaking, radiance-only measurements in O_2 B band reduce w retrieval uncertainty as much as 10% but not more than 3% for H_{peak} retrieval, compared with radiance-only O_2 A band measurements.

In summary, adding multi-angle radiance-only measurements in O_2 B band improve w retrieval more than H_{peak} , while DOLP measurements in O_2 B band are more useful for H_{peak} retrieval. Over vegetation, the improvement from O_2 B radiance measurements is greater than for the other surfaces. When H_{peak} increases and is larger than 2 km, O_2 B DOLP causes less uncertainty reduction of H_{peak} but more for w . The improvement of O_2 B both radiance and DOLP depends more than radiance-only O_2 B measurements on the number of angles used in multi-angle retrieval.

5.4. Each posterior uncertainty component

As described in Eq. (2)–(4), besides the prior uncertainty of the state vector itself (S_a), the posterior uncertainty in ALH parameters (\hat{S}) also depends on the measurement uncertainty (S_y) and forward model parameter uncertainty (S_b). In this section, the contribution from each source of the posterior uncertainty except the prior un-

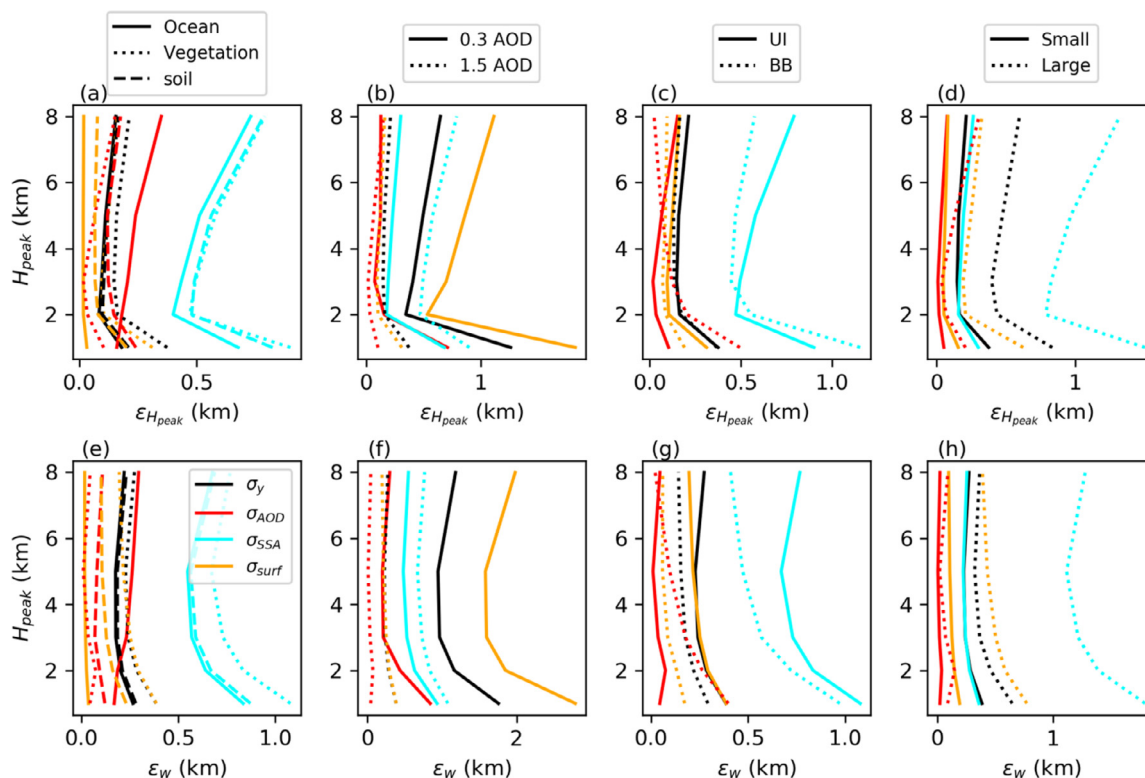


Fig. 10. The variation of posterior uncertainty for H_{peak} ($\varepsilon_{H_{\text{peak}}}$) and w (ε_w) with H_{peak} due to the measurement uncertainty (σ_y), uncertainties of AOD (σ_{AOD}) and SSA (σ_{SSA}) and surface model parameters (σ_{surf}). In each panel, $\varepsilon_{H_{\text{peak}}}$ or ε_w from different error sources is shown as different colored lines, and different line styles indicate different surface types (a and e), different aerosol types (b and f), different aerosol types (c and g) and different magnitudes of uncertainties for each error source. For each panel, only one factor changes, while other factors are kept constant, such as 1.5 AOD, vegetation, UI aerosol type, 2% measurements uncertainty, 10% uncertainties of AOD and surface parameters and 3% SSA uncertainty. For the last column (d and h), small uncertainty means 2% for measurement uncertainty, 5% for AOD and surface parameters and 1% for SSA, while large uncertainty means 10%, 20% and 5% for these four error sources, respectively.

certainty is analyzed. Firstly, we compare the influence of different simulation factors, such as surface type, aerosol types and AOD, on each error component. Then, the uncertainties in different observation scenarios in Table 3 are compared.

Based on the assumed uncertainties of three types of model parameters including AOD (σ_{AOD}), SSA (σ_{SSA}) and surface BRDF/BPDF kernel coefficients (σ_{surf}), we compare in Fig. 10 (shown as different colored lines) the retrieval uncertainty of H_{peak} and w resulting from each of these three error sources, as well as the uncertainty of observed radiance and DOLP (σ_y) for MAPMO observations (AB-IP cases). Each error source causes the lowest H_{peak} posterior uncertainty ($\varepsilon_{H_{\text{peak}}}$) at 2 km H_{peak} and the lowest w uncertainty (ε_w) at 3–5 km H_{peak} . The largest uncertainties of both H_{peak} and w appear at 1 km H_{peak} , while $\varepsilon_{H_{\text{peak}}}$ increases with increasing H_{peak} for $H_{\text{peak}} > 2$ km but ε_w changes little. In general, the same uncertainty of each error source causes equal or larger uncertainty for w than for H_{peak} .

In each panel of Fig. 10, only one factor of the simulation scenario changes, and the posterior uncertainty from four error sources are compared. In the first column of Fig. 10, the uncertainties over three surface types are compared. $\varepsilon_{H_{\text{peak}}}$ due to SSA uncertainty is similar over vegetation and soil, but ~ 0.1 km smaller over ocean, maintaining the same distribution at different H_{peak} (Fig. 10a). However, the ε_w induced by SSA uncertainty over vegetation is around 0.3 km larger than for ocean and soil, indicating the larger impact of SSA uncertainty on w retrieval over vegetation (Fig. 10e). Focusing on uncertainties from σ_y , both $\varepsilon_{H_{\text{peak}}}$ and ε_w show little difference over ocean and soil, but have 0.1–0.2 km more uncertainty over vegetation. In addition, σ_{surf} induces the largest uncertainty over vegetation, less uncertainty over soil and

the lowest uncertainty over ocean, where the differences are 0.1–0.2 km in both $\varepsilon_{H_{\text{peak}}}$ and ε_w . Different with other three error sources, AOD uncertainty leads to different variations of $\varepsilon_{H_{\text{peak}}}$ (or ε_w) with H_{peak} over different types of surface, resulting in larger difference of $\varepsilon_{H_{\text{peak}}}$ (or ε_w) between three surface types at higher H_{peak} . Comparing the uncertainties from σ_{AOD} , σ_y and σ_{surf} , over ocean σ_{AOD} induces the largest uncertainty, σ_y induces less uncertainty, and σ_{surf} causes little uncertainty in ALH retrieval. Over soil, these three error sources lead to similar H_{peak} and w uncertainties, while over vegetations σ_y and σ_{surf} result in larger uncertainty than σ_{AOD} . σ_{SSA} always causes the largest uncertainty for each surface type.

Using retrievals over vegetation as an example, the second, third and fourth columns of Fig. 10 show the impact of different AOD, aerosol types and uncertainties of each error source on the four components of the posterior uncertainty of H_{peak} and w . When AOD decreases from 1.5 to 0.3, only σ_{SSA} induced uncertainties decrease while the other three uncertainties increase (Fig. 10b and 10f); σ_{surf} induced uncertainties change most with 0.5–1.5 km $\varepsilon_{H_{\text{peak}}}$ difference, while uncertainties from σ_y and σ_{AOD} increase 0.2–1.0 km and less than 0.7 km, respectively (Fig. 10b). Except σ_{SSA} , other three error sources cause similar $\varepsilon_{H_{\text{peak}}}$ (or ε_w) at large AOD, but differ a lot at small AOD (Fig. 10b and 10f). Comparing different aerosol types, σ_{SSA} and σ_{AOD} lead to greater $\varepsilon_{H_{\text{peak}}}$ for BB than UI at low H_{peak} , but less at higher H_{peak} , with as much as 0.3–0.4 km uncertainty difference. In contrast, the $\varepsilon_{H_{\text{peak}}}$ from σ_y and σ_{surf} show little distinction between UI and BB (Fig. 10c). Unlike $\varepsilon_{H_{\text{peak}}}$, ε_w from σ_{AOD} for BB is larger than UI at all H_{peak} , while the other three error sources result in less ε_w for BB than

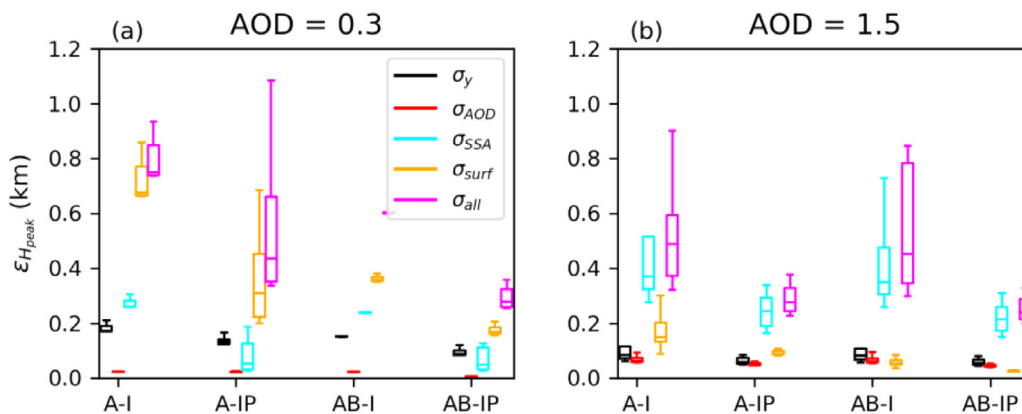


Fig. 11. The posterior uncertainty for H_{peak} ($\varepsilon_{H_{\text{peak}}}$) from uncertainties of measurements (σ_y), AOD (σ_{AOD}), SSA (σ_{SSA}), surface model parameters (σ_{surf}) and all of these at 0.3 AOD and 1.5 AOD for scenario A-I (O_2 A I), A-IP (O_2 A I+P), AB-I (O_2 A + B I) and AB-IP (O_2 A + B I+P), shown as the x-axis labels. Each box represents the distribution of posterior uncertainty when different number of angles are used in the retrieval, similar to Fig. 8a-8c. The cases here are for BB aerosol at 3 km H_{peak} and 1 km w .

UI. The difference caused by different aerosol types in the four error components of ε_w is not more than 0.4 km (Fig. 10g). Finally, in Fig. 10d and 10h we show the influence on ALH retrieval of increasing σ_{SSA} , σ_y , σ_{AOD} and σ_{surf} . If σ_{SSA} increases from 1% (small) to 5% (large), the $\varepsilon_{H_{\text{peak}}}$ and ε_w increase 0.7–1.2 km and 1.0–1.4 km, respectively. Similarly, a change of σ_y from 2% to 10% and σ_{surf} from 5% to 20% lead to 0.3–0.4 km and 0.2–0.5 km $\varepsilon_{H_{\text{peak}}}$ difference, respectively. Increasing σ_{AOD} from 5% to 20% has little influence on $\varepsilon_{H_{\text{peak}}}$ and ε_w . However, the value of AOD has the largest impact on the $\varepsilon_{H_{\text{peak}}}$ and ε_w from different error sources.

Furthermore, in Fig. 11, we compare the $\varepsilon_{H_{\text{peak}}}$ from four error sources for different observation scenarios including A-I, A-IP, AB-I and AB-IP, as well as the total errors. Here, the x-axis represents these four scenarios, and each box shows different uncertainties when the number of angles increases from one to nine in multi-angle retrieval. If AOD is small (Fig. 11a), from radiance-only O_2 A observations (A-I), σ_{surf} causes the largest uncertainty in H_{peak} and dominates its total posterior uncertainty, decreasing from 0.85 km to 0.65 km when adding more angles to the retrieval. Then, σ_{SSA} and σ_y can induce 0.3–0.35 km and 0.2 km $\varepsilon_{H_{\text{peak}}}$, respectively, while σ_{AOD} leads to the lowest $\varepsilon_{H_{\text{peak}}}$ (< 0.05 km). When adding DOLP measurements in O_2 A band (A-IP), the comparison between $\varepsilon_{H_{\text{peak}}}$ from four error sources remains similar, but each error component decreases, as much as 0.45 km for σ_{surf} -induced $\varepsilon_{H_{\text{peak}}}$. By comparing scenarios AB-I and A-I, adding radiance-only measurements in O_2 B band to MAIA observations, the $\varepsilon_{H_{\text{peak}}}$ from σ_{AOD} , σ_y and σ_{SSA} decreases slightly, < 0.05 km, and mainly for smaller number of angles retrieval with larger uncertainty, whereas σ_{surf} induced $\varepsilon_{H_{\text{peak}}}$ is reduced more than 0.25 km. The effect of adding both radiance and DOLP in O_2 B band is similar like O_2 B radiance-only measurements (compare A-IP and AB-IP). At large AOD (Fig. 11b), σ_{SSA} induces the largest uncertainty, and dominates the total posterior uncertainty instead of σ_{surf} , while uncertainties from σ_{AOD} and σ_y are generally the lowest. Similarly, magnitude of ε_w also shows similar patterns with $\varepsilon_{H_{\text{peak}}}$, but with higher values for each error component. Adding polarized measurements can reduce uncertainties from all sources significantly, while O_2 B radiance measurements mainly improve the uncertainties resulting from uncertainty from surface reflectance, for both ALH parameters and for different AOD or aerosol types.

6. Conclusions and discussion

In this study, we investigated theoretically the capability to retrieve ALH from multi-angle polarization measurements in both O_2 A and B absorption bands from space. Based on the design of MAIA, which only detects TOA radiance from multiple angles in O_2 A band, a hypothetical sensor called MAPMO is defined by improving the capability of a MAIA-like instrument to observe both radiance and polarization in the O_2 A and B bands. By applying optimal estimation theory, this study quantified the information content from simulated satellite measurements for both MAIA and MAPMO, in terms of the degree of freedom for signal (DFS) for two aerosol vertical distribution parameters, H_{peak} and w . In addition, the retrieval uncertainties of H_{peak} and w were estimated and compared, from the uncertainties of not only the instrument but also model uncertainties due to the parameters such as AOD, SSA and surface model coefficients not retrieved from O_2 absorption bands. The TOA radiance and degree of linear polarization, as well as their Jacobians with respect to H_{peak} and w , were simulated by our forward model UNL-VRM - a vector radiative transfer code with surface bidirectional reflectance distribution function (BRDF) and surface polarized reflectance (BPDF) function considered. The information content analysis is conducted for different aerosol types, AOD, and surface reflectance as a function of number of viewing angles, which enables different comparison studies focusing on the impacts of multiple angles and O_2 B band on the retrievals of H_{peak} and w between different observation scenarios.

We found that for either MAIA or MAPMO measurements, the lowest H_{peak} and w information content are provided over vegetation due to its high surface reflectance in O_2 A band, and aerosol optical property influences ALH information less than the surface reflectance. Compared with H_{peak} , whose DFS is high (> 0.8) in all scenarios, the w DFS is smaller. More measurements from different angles in general add more information content for H_{peak} and w , but there is a limit, and following around six angles there appears to be little benefit in adding more in the retrieval. While the angular-dependence of DFS for either H_{peak} or w is similar between MAIA and MAPMO, MAPMO consistently shows higher DFS for both H_{peak} and w , especially over vegetation at lower AOD for H_{peak} or larger AOD for w . DFS for H_{peak} and w generally increases with AOD, and the impact of AOD on w DFS is greater than its impact on H_{peak} . Because MAPMO has much richer information for H_{peak} than MAIA does, MAPMO's retrieval of H_{peak} is more robust with respect to the change of AOD.

Compared with single-angle measurement in O₂ A band, adding radiance measurements from nine viewing angles improves H_{peak} retrieval most at 2–3 km H_{peak}, but improves w retrieval more at the boundary layer or upper troposphere. When AOD increases, this improvement decreases for H_{peak} but increases for w, indicating that multiple angles are more effective to w retrieval at larger AOD. Among different surface types, the multi-angle improvement is the strongest over vegetation for H_{peak} but over ocean for w. If polarized measurements are added, this multi-angle improvement in O₂ A band is similar among the three types of surface for H_{peak}, but still strongest over ocean for w, especially at low AOD. Generally, variation of AOD has a bigger impact on the multi-angle improvement for w than for H_{peak}. Comparing the two O₂ bands, improvement from multi-angle measurements is bigger for w retrievals in O₂ A band than O₂ B band, but multi-angle measurements including polarization improve H_{peak} retrievals more with O₂ B band than O₂ A band.

When MAIA-like measurements are improved by adding the capability to observe TOA polarization in O₂ A band, the posterior uncertainty of w is reduced more than H_{peak}, while the uncertainty reductions of both H_{peak} and w are larger over ocean and soil than vegetation. When more angles are used, this uncertainty reduction due to polarized measurements is greater, especially for ocean and soil surfaces. Furthermore, polarized measurements reduce H_{peak} uncertainty more when H_{peak} decreases over ocean and soil, but the uncertainty reduction is the largest at 2–3 km over vegetation. When adding multi-angle measurements of O₂ B band together with O₂ A band observations, the posterior uncertainties of H_{peak} and w are reduced largely for vegetation surface due to the smaller surface reflectance in O₂ B band than O₂ A band. Compared with the radiance-only measurements in O₂ B band, O₂ B DOLP shows effective improvement for the H_{peak} retrieval, but is less useful for w. Both radiance and polarized measurements in O₂ B band effectively improve H_{peak} retrieval for cases with lower H_{peak}, while effectively improve w retrieval for cases with high H_{peak}.

In terms of retrieval error budget, uncertainty in SSA always causes the largest uncertainty at large AOD for both H_{peak} and w retrievals, whereas at small AOD the retrieval uncertainty from the uncertainties of surface model parameters is the largest. Compared with varying aerosol optical property, surface reflectance or uncertainty of each error source, changing AOD causes the largest impact on the four error components. Regardless of sources of errors, H_{peak} has the least uncertainty for H_{peak} at ~2 km, and for w at H_{peak} of 3–5 km; for same source of error, it induces larger uncertainty in w retrieval than H_{peak} retrieval. Compared with polarized measurements in O₂ A or O₂ B which reduce all uncertainties significantly, adding radiance measurements in O₂ B band into O₂ A radiance measurements mainly reduces the uncertainty resulting from surface uncertainty, with little impact on uncertainties from other sources.

In summary, compared with single-angle measurements in O₂ A band, adding polarized measurements or multi-angle measurements improves ALH retrieval effectively. However, if only one type of measurement could be added, without consideration of technical issues, multi-angle measurements are recommended instead of polarization considering all surface types. For multi-angle measurements, if only two channels can be provided by the sensor, observing O₂ A band radiance and polarization is recommended, rather than O₂ B radiance and polarized measurements or O₂ A and B radiances. When three channels are available, O₂ A radiance and polarized measurements combined with O₂ B radiances provide more ALH information. Obviously, all four channels including radiance and polarized measurements in two O₂ bands together improve ALH retrieval the most compared with single-channel measurements, especially for a vegetated surface. Although ALH information between various types of aerosols show some distinc-

tion because of their different single-scattering optical properties, the dependence of information on surface types and the impact of multi-angle and/or polarized measurements generally appear similar. The information and error analysis in this study provides a theoretical foundation for the design of a future satellite-based passive multi-angle sensor dedicated to observing aerosol height.

Declaration of Competing Interest

The authors declare that they have no known competing financial interests or personal relationships that could have appeared to influence the work reported in this paper.

CRediT authorship contribution statement

Xi Chen: Software, Formal analysis, Writing - original draft, Investigation, Visualization. **Xiaoguang Xu:** Software, Writing - review & editing, Resources. **Jun Wang:** Conceptualization, Investigation, Writing - original draft, Supervision. **David J. Diner:** Writing - review & editing, Supervision, Project administration.

Acknowledgement

This study is supported by NASA MAIA project and Remote Sensing Theory program (Grant No.: 80NSSC20K1747). We thank the MAIA science team for their constructive suggestions and fruitful discussions. The High-Performance Computing group at University of Iowa is acknowledged for the computational support.

Appendix

As described in the main text, based on the assumption that the correlation between measurements from different viewing angles decreases from the closest to the farthest pair of angles, the correlation coefficients between the angle Da and other angles are defined from 1.0 to 0.0 for angle Da to angle Df with an equal reduction of 1/8. Moreover, the radiance and DOLP measurement errors have no correlations, regardless of angle. Thus, the correlation coefficient matrix (C) in one O₂ absorption band is defined as shown in Fig. A1. Similarly, the measurement errors in O₂ B band are assumed following the same correlation coefficients as those in O₂ A band. However, when considering the retrieval including measurements in both O₂ A and B band, they are independent with

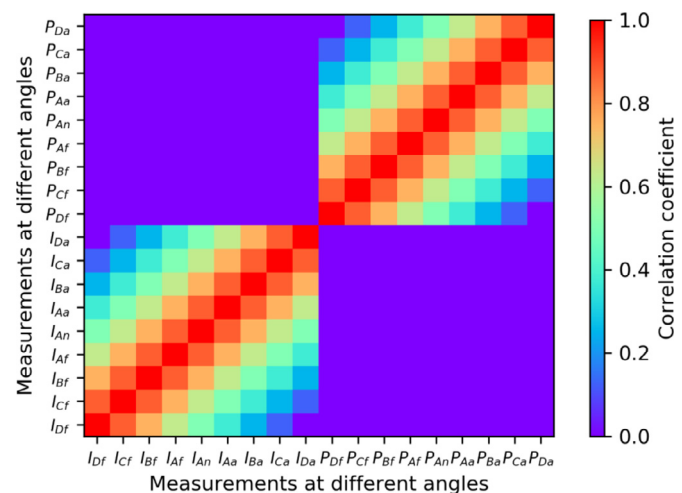


Fig. A1. The correlation coefficient matrix expressed as (C) in Section 3.2.2 for multi-angle radiance and polarized measurements in O₂ A band. In x-axis and y-axis, I represents the radiance measurement and P is DOLP, and the subscript of I and P indicates the viewing angle described in Fig. 2a.

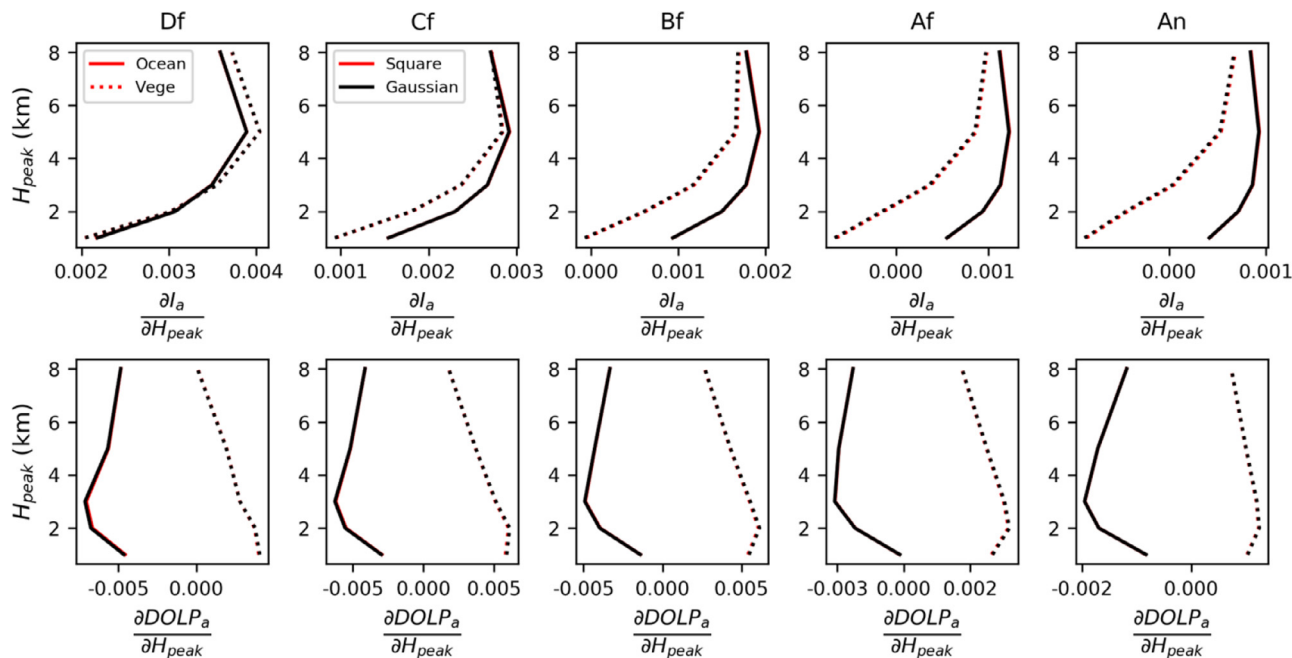


Fig. A2. The comparison of convolved Jacobians at five viewing angles over ocean and vegetation between using square and Gaussian spectral response function assumption. The other parameters describing simulation scenario are the same as Fig. 4a.

each other. As a consequence, the total correlation coefficient matrix (C_2) of both O_2 A and B band measurement errors are defined as:

$$C_2 = \begin{bmatrix} 0 & C_A \\ C_B & 0 \end{bmatrix}.$$

Here, C_A and C_B represent the correlation coefficient matrix in O_2 A and B band, respectively. Thus, $C_A = C_B$ and both are the same as shown in Fig. A1. 0 shows the zero matrix having the same shape as C_A and C_B .

The square response function assumption used in this study could result in larger weights for channels close to the band edge compared with Gaussian response function. This may affect the convolved TOA reflectance and its Jacobians in O_2 absorption bands. We supplemented the comparison of the convolved Jacobians in O_2 A band using square and Gaussian response function in the following figure (Fig. A2). Five viewing angles and two surface types (ocean and vegetation) are selected as examples and other parameters are the same to Fig. 2 in the manuscript. Comparing the red and black lines, it is found that these two response functions cause little difference in the convolved Jacobians and the resultant DFS difference is negligible. In fact, the Jacobians differences are less than 1%. Thus, even though our square response function is not realistic, it will not affect our estimation of ALH information from simulated satellite measurements.

When we discuss the improvement of multi-angle measurements in ALH retrieval compared with single-angle measurement, all the cases in Fig. 7 are for BB aerosol, while the error reductions for UI aerosol are shown in Fig. A3. The dependence of multi-

angle measurements improvement in both O_2 A and B band on the number of angles are similar to BB aerosol, but the improvement is greater for H_{peak} retrieval from adding DOLP measurements. For parameter w , the multi-angle radiance only measurements improve less for UI aerosol than BB aerosol, the same as multi-angle polarized measurements at smaller AOD, but improve more for polarized measurements at larger AOD.

When the w varies, how the posterior uncertainty from multi-angle measurements in O_2 A band changes is shown in Fig. A4. The posterior errors of H_{peak} and w demonstrate the opposite patterns that H_{peak} error is the lowest if w is 0.5–1 km, while w displays the highest error for this w range. The error reduction by adding polarization in O_2 A band to radiance-only retrieval also shows similar variation with w . This improvement is the largest for w retrieval at 0.5–1 km w but the lowest for H_{peak} . As a result, when w ranges from 0.5 km to 1 km, the O_2 A band measurement can provide larger information for H_{peak} but lower for w . In this circumstance, the improvement of polarization in O_2 A band is the strongest for w but opposite for H_{peak} .

Similar to Fig. 11, the four error sources caused posterior errors, as well as their total posterior errors for UI aerosol are shown in Fig. A5. Compared with BB aerosol, similar patterns of four error components are found for UI aerosol, as well as the same dominated error source, but with larger values, especially at smaller AOD (Fig. A5a). The polarized measurements reduce UI errors more than BB at smaller AOD, but similar at larger AOD. In summary, the roles of polarized measurements and O_2 B measurements in ALH retrieval are the same between different aerosol types.

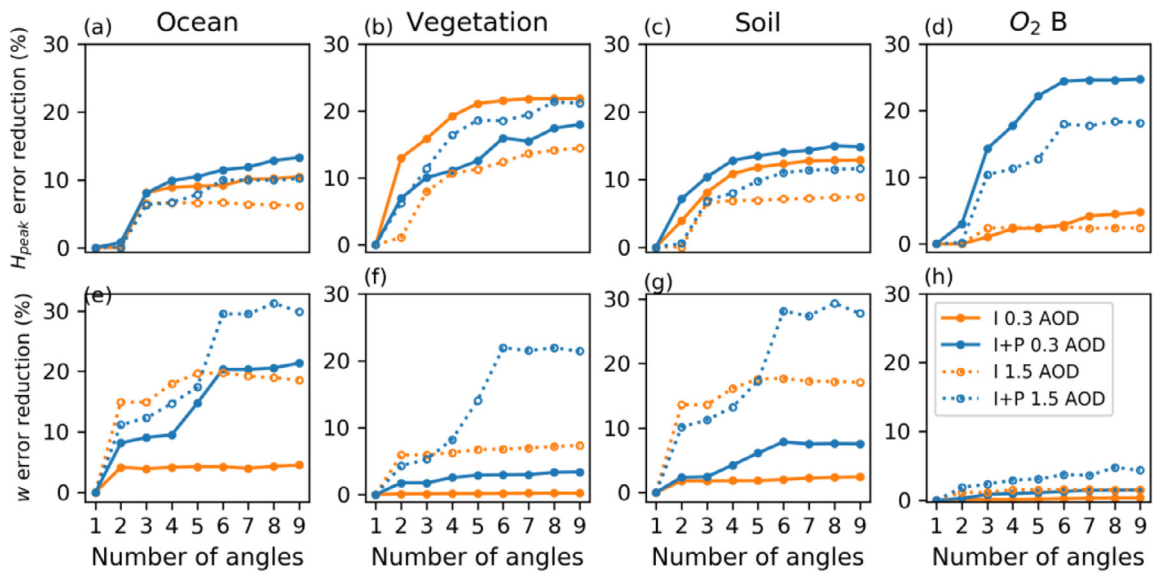


Fig. A3. Similar to Fig. 7 but for UI aerosol.

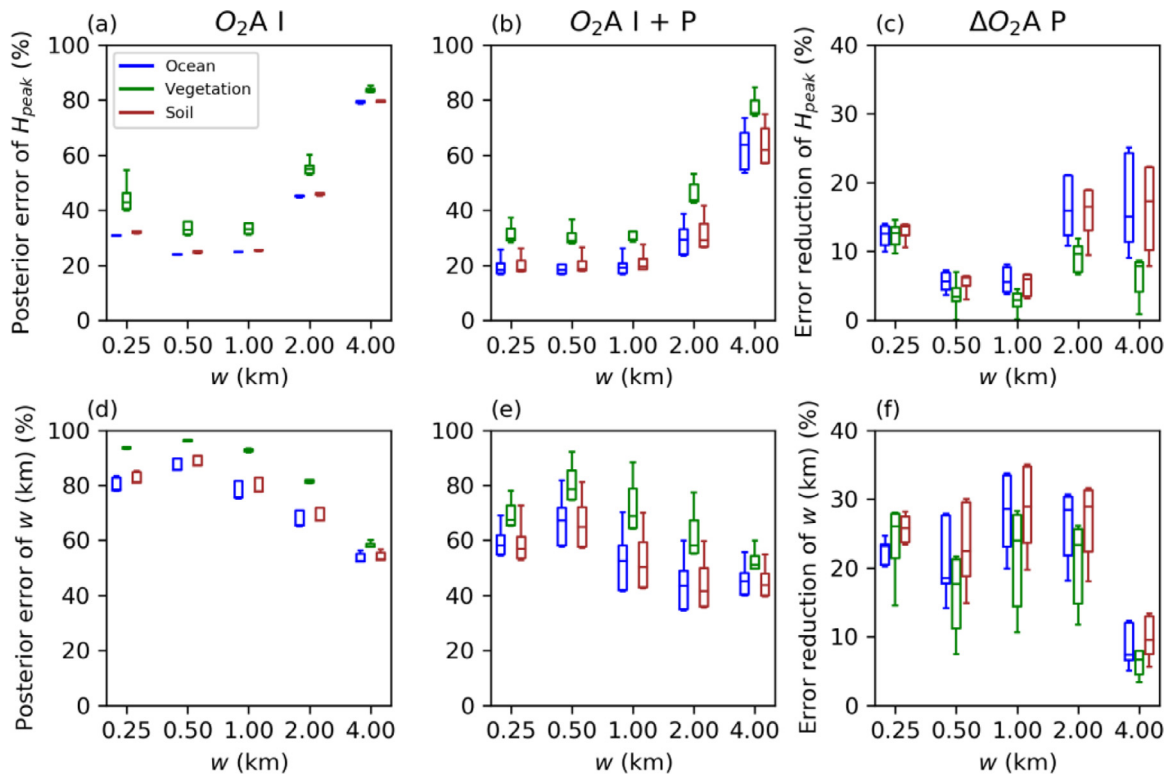


Fig. A4. Similar to Fig. 8 but varies with w values. The H_{peak} here is fixed as 3 km.

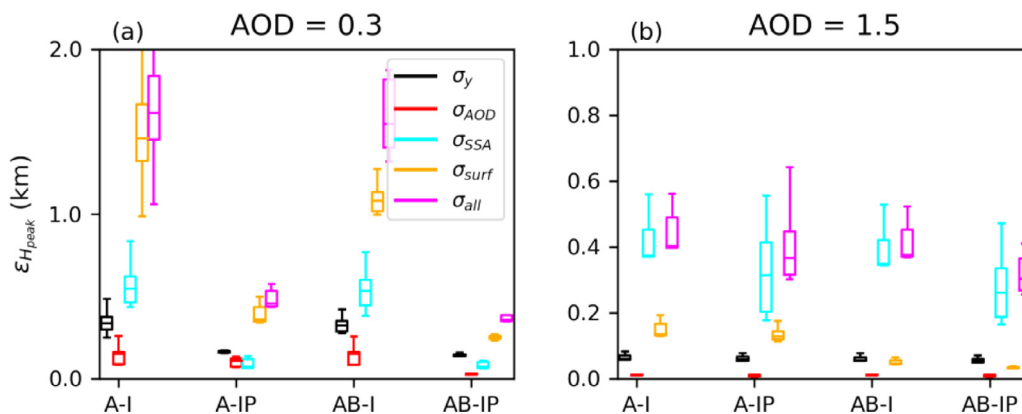


Fig. A5. Similar to Fig. 11 but for UI aerosol.

References

- [1] Boesche E, Stammes P, Bennartz R. Aerosol influence on polarization and intensity in near-infrared O₂ and CO₂ absorption bands observed from space. *J Quant Spectrosc Radiat Transfer* 2009;110:223–39.
- [2] Chen X, Y. Liu, D. Yang, Z. Cai, H. Chen, and M. Wang, 2019: A Theoretical Analysis for Improving Aerosol-Induced CO₂ Retrieval Uncertainties Over Land Based on TanSat Nadir Observations Under Clear Sky Conditions. *Remote Sensing*, 11, 1061.
- [3] Chen X, Wang J, Liu Y, Xu X, Cai Z, Yang D, et al. Angular dependence of aerosol information content in CAPI/TanSat observation over land: Effect of polarization and synergy with A-train satellites. *Remote Sens Environ* 2017;196:163–77.
- [4] Choi M, Sander SP, Spurr RJD, Pongetti TJ, et al. Aerosol profiling using radiometric and polarimetric spectral measurements in the O₂ near infrared bands: estimation of information content and measurement uncertainties. *Remote Sens Environ* 2021:253.
- [5] Christian K, Wang J, Ge C, Peterson D, Hyer E, Yorks J, McGill M. Radiative Forcing and Stratospheric Warming of Pyrocumulonimbus Smoke Aerosols: First Modeling Results With Multisensor (EPIC, CALIPSO, and CATS) Views from Space. *Geophys Res Lett* 2019;46:10061–71.
- [6] Davis AB, Kalashnikova OV. Aerosol layer height over water via Oxygen a-band observations from space: a tutorial. In: *Springer Series in Light Scattering: Volume 3: Radiative Transfer and Light Scattering*, A. Kokhanovsky. Springer International Publishing; 2019. p. 133–66.
- [7] Diner D, Boland SW, Brauer M, Bruegge C, Burke KA, Chipman RA, et al. Advances in multiangle satellite remote sensing of speciated airborne particulate matter and association with adverse health effects: from MISR to MAIA. *J Appl Remote Sens* 2018;12:042603.
- [8] Diner DJ, Davis A, Hancock B, Gutt G, Chipman RA, Cairns B. Dual-photoelastic-modulator-based polarimetric imaging concept for aerosol remote sensing. *Appl Opt* 2007;46:8428–45.
- [9] Diner DJ, Davis AB, Hancock B, Geier S, Rheingans B, Jovanovic V. First results from a dual photoelastic-modulator-based polarimetric camera. *Appl Opt* 2010;49:2929–46.
- [10] Ding S, Wang J, Xu X. Polarimetric remote sensing in oxygen A and B bands: sensitivity study and information content analysis for vertical profile of aerosols. *Atmos. Meas. Tech.* 2016;9:2077–92.
- [11] Dubovik O, Smirnov A, Holben BN, King MD, Kaufman YJ, Eck TF, Slutsker I. Accuracy assessments of aerosol optical properties retrieved from Aerosol Robotic Network (AERONET) Sun and sky radiance measurements. *J Geophys Res: Atmos* 2000;105:9791–806.
- [12] Dubovik O, Holben B, Eck T, Smirnov A, Kaufman YJ, King MD, et al. Variability of absorption and optical properties of key aerosol types observed in worldwide locations. *J Atmospheric Sci* 2002;59:590–608.
- [13] Dubovik O, Herman M, Holdak A, Lapyonok T, Tanré D, Deuzé JL, et al. Statistically optimized inversion algorithm for enhanced retrieval of aerosol properties from spectral multi-angle polarimetric satellite observations. *Atmos Meas Tech* 2011;4:975–1018.
- [14] Dubuisson P, Frouin R, Dessailly D, Duforêt L, Léon J-F, Voss K, Antoine D. Estimating the altitude of aerosol plumes over the ocean from reflectance ratio measurements in the O₂ A-band. *Remote Sens Environ* 2009;113:1899–911.
- [15] Frankenberg C, Hasekamp O, O'Dell C, Sanghavi S, Butz A, Worden J. Aerosol information content analysis of multi-angle high spectral resolution measurements and its benefit for high accuracy greenhouse gas retrievals. *Atmos Meas Tech* 2012;5:1809–21.
- [16] Geddes A, Bösch H. Tropospheric aerosol profile information from high-resolution oxygen A-band measurements from space. *Atmos Meas Tech* 2015;8:859–74.
- [17] Griffin D, Sioris C, Chen J, Dickson N, Kovachik A, et al. The 2018 fire season in North America as seen by TROPOMI: aerosol layer height validation and evaluation of model-derived plume heights. *Atmos Meas Tech Discuss* 2019:1–30 2019.
- [18] Hasekamp OP, Litvinov P, Butz A. Aerosol properties over the ocean from PARASOL multiangle photopolarimetric measurements. *J Geophys Res* 2011:116.
- [19] Hasekamp OP, Fu G, Rusli SP, et al. Aerosol measurements by SPEXone on the NASA PACE mission: expected retrieval capabilities. *J Quant Spectrosc Radiat Transfer* 2019;227:170–84.
- [20] Hou W, Wang J, Xu X, Reid JS. An algorithm for hyperspectral remote sensing of aerosols: 2. Information content analysis for aerosol parameters and principal components of surface spectra. *J Quant Spectrosc Radiat Transfer* 2017;192:14–29.
- [21] Kahn RA, Gaitley BJ. An analysis of global aerosol type as retrieved by MISR. *J Geophys Res: Atmos* 2015;120:4248–81.
- [22] Kokhanovsky AA, Rozanov VV. The determination of dust cloud altitudes from a satellite using hyperspectral measurements in the gaseous absorption band. *Int J Remote Sens* 2010;31:2729–44.
- [23] Levy RC, Remer LA, Mattoo S, Vermote EF, Kaufman YJ. Second-generation operational algorithm: retrieval of aerosol properties over land from inversion of moderate resolution imaging Spectroradiometer spectral reflectance. *J Geophys Res: Atmos* 2007;112:1–21.
- [24] Litvinov P, Hasekamp O, Cairns B. Models for surface reflection of radiance and polarized radiance: Comparison with airborne multi-angle photopolarimetric measurements and implications for modeling top-of-atmosphere measurements. *Remote Sens Environ* 2011;115:781–92.
- [25] Litvinov P, Hasekamp O, Cairns B, Mishchenko M. Reflection models for soil and vegetation surfaces from multiple-viewing angle photopolarimetric measurements. *J Quant Spectrosc Radiat Transfer* 2010;111:529–39.
- [26] Mishchenko MI, Travis LD. Satellite retrieval of aerosol properties over the ocean using polarization as well as intensity of reflected sunlight. *J Geophys Res: Atmos* 1997;102:16989–7013.
- [27] Mlawer EJ, Payne VH, Moncet J-L, Delamere JS, Alvarado MJ, Tobin DC. Development and recent evaluation of the MT_CKD model of continuum absorption. *Philos Trans R Soc, A* 2012;370:2520–56.
- [28] Nanda S, de Graaf M, Veefkind JP, Sneep M, ter Linden M, Sun J, Levelt PF. Validating TROPOMI aerosol layer height retrievals with CALIOP data. *Atmos Meas Tech* 2019.
- [29] Nelson DL, Garay MJ, Kahn RA, Dunst BA. Stereoscopic height and wind retrievals for aerosol plumes with the MISR Interactive Explorer (MINX). *Remote Sens* 2013;5:4593–628.
- [30] Peters K, Quaas J, Bellouin N. Effects of absorbing aerosols in cloudy skies: a satellite study over the Atlantic Ocean. *Atmos Chem Phys* 2011;11:1393–404.
- [31] Reid JS, Jonsson HH, Maring HB, et al. Comparison of size and morphological measurements of coarse mode dust particles from Africa. *J Geophys Res: Atmos* 2003:108.
- [32] Rodgers CD. *Inverse Methods for Atmospheric Sounding: Theory and Practice*. World Scientific Publishing Co Pte Ltd; 2000.
- [33] Rothman LS, Gordon IE, Babikov Y, et al. The HITRAN2012 molecular spectroscopic database. *J Quant Spectrosc Radiat Transfer* 2013;130:4–50.
- [34] Sanders AFJ, de Haan JF, Sneep M, et al. Evaluation of the operational Aerosol Layer Height retrieval algorithm for Sentinel-5 Precursor: application to O₂ A band observations from GOME-2A. *Atmos Meas Tech* 2015;8:4947–77.
- [35] Sanghavi S, Martonchik JV, Landgraf J, Platt U. Retrieval of the optical depth and vertical distribution of particulate scatterers in the atmosphere using O₂ A- and B-band SCIAMACHY observations over Kanpur: a case study. *Atmos Meas Tech* 2012;5:1099–119.
- [36] Sanghavi S, Nelson R, Frankenberg C, Gunson M. Aerosols in OCO-2/GOSAT retrievals of XCO₂: An information content and error analysis. *Remote Sens Environ* 2020:251.
- [37] Schaaf CB, Gao F, Strahler AH, et al. First operational BRDF, albedo nadir reflectance products from MODIS. *Remote Sens Environ* 2002;83:135–48.

- [38] Torres O, Bhartia PK, Herman JR, Ahmad Z, Gleason J. Derivation of aerosol properties from satellite measurements of backscattered ultraviolet radiation: theoretical basis. *Jo Geophys Res: Atmos* 1998;103:17099–110.
- [39] Wang J, Christopher SA. Intercomparison between satellite-derived aerosol optical thickness and PM_{2.5} mass: Implications for air quality studies. *Geophys Res Lett* 2003;30.
- [40] Wang J, Xu X, Ding S, et al. A numerical testbed for remote sensing of aerosols, and its demonstration for evaluating retrieval synergy from a geostationary satellite constellation of GEO-CAPE and GOES-R. *J Quant Spectrosc Radiat Transfer* 2014;146:510–28.
- [41] Wanner W, Li X, Strahler A. On the derivation of kernels for kernel-driven models of bidirectional reflectance. *J Geophys Res: Atmos* 1995;100:21077–89.
- [42] Wanner W, Strahler AH, Hu B, et al. Global retrieval of bidirectional reflectance and albedo over land from EOS MODIS and MISR data: theory and algorithm. *J Geophys Res: Atmos* 1997;102:17143–61.
- [43] Wendisch M, Hellmuth O, Ansmann A, et al. Radiative and dynamic effects of absorbing aerosol particles over the Pearl River Delta. *China. Atmos Environ* 2008;42:6405–16.
- [44] Winker DM, Vaughan MA, Omar A, et al. Overview of the CALIPSO mission and CALIOP data processing algorithms. *J Atmos Oceanic Technol* 2009;26:2310–23.
- [45] Wu L, Hasekamp O, van Diedenhoven B, Cairns B, Yorks JE, Chowdhary J. Passive remote sensing of aerosol layer height using near-UV multiangle polarization measurements. *Geophys Res Lett* 2016;43:8783–90.
- [46] Xu F, van Harten G, Diner DJ, Kalashnikova OV, Seidel FC, Bruegge CJ, Dubovik O. Coupled retrieval of aerosol properties and land surface reflection using the airborne multiangle spectropolarimetric imager. *J Geophys Res: Atmos* 2017;122:7004–26.
- [47] Xu X, Wang J. Retrieval of aerosol microphysical properties from AERONET photopolarimetric measurements: 1. Information content analysis. *J Geophys Res: Atmos* 2015;120:7059–78.
- [48] Xu, X., J. Wang, Y. Wang, and A. Kokhanovsky, 2018: Chapter 1 - Passive Remote Sensing of Aerosol Height. *Remote Sensing of Aerosols, Clouds, and Precipitation*, T. Islam, Y. Hu, A. Kokhanovsky, and J. Wang, Eds., Elsevier, 1–22.
- [49] Xu X, Wang J, Wang Y, et al. Passive remote sensing of altitude and optical depth of dust plumes using the oxygen A and B bands: First results from EPIC/DSCOVR at Lagrange-1 point. *Geophys Res Lett* 2017;44:7544–54.
- [50] Xu X, Wang J, Wang Y, et al. Detecting layer height of smoke aerosols over vegetated land and water surfaces via oxygen absorption bands: hourly results from EPIC/DSCOVR in deep space. *Atmos Meas Tech* 2019;12:3269–88.
- [51] Yang Z, Wang J, Ichoku C, Hyer E, Zeng J. Mesoscale modeling and satellite observation of transport and mixing of smoke and dust particles over northern sub-Saharan African region. *J Geophys Res: Atmos* 2013;118 12.139–112.157.
- [52] Yokota T, Yoshida Y, Eguchi N, Ota Y, Tanaka T, Watanabe H, Maksyutov S. Global concentrations of CO₂ and CH₄ retrieved from GOSAT: first preliminary results. *Scientific online letters on the atmosphere* 2009;5:160–3.
- [53] Zeng J, Han Q, Wang J. High-spectral resolution simulation of polarization of skylight: Sensitivity to aerosol vertical profile. *Geophysical research letters*; 2008. p. 35.
- [54] Zeng Z-C, Chen S, Natraj V, et al. Constraining the vertical distribution of coastal dust aerosol using OCO-2 O₂ A-band measurements. *Remote Sens Environ* 2020:236.
- [55] Zhang L, Li QB, Gu Y, Liou KN, Meland B. Dust vertical profile impact on global radiative forcing estimation using a coupled chemical-transport-radiative-transfer model. *Atmos Chem Phys* 2013;13:7097–114.
- [56] Zhu Y, Gelaro R. Observation sensitivity calculations using the adjoint of the Gridpoint Statistical Interpolation (GSI) analysis system. *Month Weather Rev* 2008;136:335–51.
- [57] Maignan Fabienne, Bréon François-Marie, Fédèle Emilie, Bouvier Marc. Polarized reflectances of natural surfaces: Spaceborne measurements and analytical modeling. *Remote Sensing of Environment* 2009;113:2642–50.
- [58] Nadal Florence, Breon Francois-Marie. Parameterization of Surface Polarized Reflectance Derived from POLDER Spaceborne Measurements. *IEEE Transactions on Geoscience and Remote Sensing* 1999;37(3):1709–18.
- [59] Waquet F, Léon JF, Cairns B, Goloub P, Deuzé JL, Auriol F. Analysis of the spectral and angular response of the vegetated surface polarization for the purpose of aerosol remote sensing over land. *Applied Optics* 2009;48(6):1228–36.